

The dark days are overcast: Iron-bearing clouds on HD 209458 b and WASP-43 b can explain low dayside albedos

K. L. Chubb^{1,2,*} and D. Samra,^{3,*} † Ch. Helling,^{3,4} L. Carone,³ and D. M. Stam.⁵

¹University of Bristol, School of Physics, Tyndall Avenue, Bristol, BS8 1TL, UK

²Centre for Exoplanet Science, University of St Andrews, North Haugh, St Andrews, KY16 9SS, UK

³Space Research Institute, Austrian Academy of Sciences, Schmiedlstr. 6, A-8042, Graz, Austria

⁴Fakultät für Mathematik, Physik und Geodäsie, TU Graz, Petersgasse 16, Graz, A-8010, Austria

⁵Leiden Observatory, Niels Bohrweg 2, 2333 CA Leiden, Netherlands

*: these authors contributed equally to this work

Accepted XXX. Received YYY; in original form ZZZ

ABSTRACT

We simulate the geometric albedo spectra of hot Jupiter exoplanets HD 209458 b and WASP-43 b, based on global climate model (GCMs) post-processed with kinetic cloud models. We predict WASP-43 b to be cloudy throughout its dayside, while HD 209458 b has a clear upper atmosphere around the hot sub-solar point, largely due to the inclusion of strong optical absorbers TiO and VO in the GCM for the latter causes a temperature inversion. In both cases our models find low geometric albedos - 0.026 for WASP-43b and 0.028 for HD 209458 b when averaged over the CHEOPS bandpass of $\sim 0.35 - 1.1 \mu\text{m}$ - indicating dark daysides, similar to the low albedos measured by observations. We demonstrate the strong impact of clouds that contain Fe-bearing species on the modelled geometric albedos; without Fe-bearing species forming in the clouds, the albedos of both planets would be much higher (0.518 for WASP-43 b, 1.37 for HD 209458 b). We conclude that a cloudy upper or mid-to-lower atmosphere that contains strongly absorbing Fe-bearing aerosol species, is an alternative to a cloud-free atmosphere in explaining the low dayside albedos of hot Jupiter atmospheres such as HD 209458 b and WASP-43 b.

Key words: planets and satellites: individual: HD 209458 b - planets and satellites: individual: WASP-43 b - planets and satellites: atmospheres - planets and satellites: gaseous planets - planets and satellites: fundamental parameters

1 INTRODUCTION

The geometric albedo of a transiting exoplanet can be inferred by observing the star and the planet just before (or after) and during the planet’s secondary eclipse. It is a measure of how reflective a planet is to incoming stellar radiation. Although this albedo is wavelength dependent, it is typically measured as an average over the bandpass of the instrument used for observation (see, for example, [Krenn et al. \(2023\)](#)). There have been several observations to infer the geometric albedos of hot giant transiting exoplanets, and with a couple of exceptions, the observed albedos are generally low, indicating dark, poorly reflective daysides. For example, the geometric albedos of a population of around 20 hot gaseous exoplanets have been measured by studies such as [Angerhausen et al. \(2015\)](#) and [Esteves et al. \(2015\)](#), with the finding that the majority have albedos typically less than 0.15 in the Kepler bandpass (0.42 - 0.91 μm). [Krenn et al. \(2023\)](#) confirm these findings by deriving a geometric albedo, A_g , of 0.076 ± 0.016 for HD 189733 b from data of the

CHARacterising EXoplanet Satellite (CHEOPS) ($\sim 0.35 - 1.1 \mu\text{m}$). This value is consistent with that previously inferred by [Evans et al. \(2013\)](#) from their HST STIS secondary eclipse measurements of HD 189733 b; they found $A_g = 0.4 \pm 0.12$ for the 0.29 - 0.45 μm region and $A_g \leq 0.12$ for the 0.45 - 0.57 μm region. The decrease of this albedo towards longer wavelengths was interpreted as being due to absorption by sodium. Some slightly higher values inferred from observations include $A_g = 0.2 \pm 0.04$ for WASP-19b using TESS (0.6 - 1.0 μm) ([Korth & Parviainen 2024](#)), 0.225 ± 0.004 for HAT-P-7b ([Heng & Demory 2013](#)), and $A_g < 0.33$ for WASP-80 b using the WFC3 instrument onboard HST ([Jacobs et al. 2023](#)). For Kepler-7b $A_g = 0.25^{+0.01}_{-0.02}$ ([Heng et al. 2021](#)), and for WASP-178b $0.1 < A_g < 0.35$ using CHEOPS ([Pagano et al. 2023](#)). A noticeable exception with a much higher measured albedo is LTT 9779 b with $A_g = 0.8^{+0.10}_{-0.17}$ ([Hoyer et al. 2023](#)). For comparison, the geometric albedo of Jupiter is around 0.44 from 0.4 - 17 μm ([Li et al. 2018](#)).

HD 209458 b (discovered by [Charbonneau et al. 2000](#)) and WASP-43 b (discovered by [Hellier et al. 2011](#)) are both hot Jupiters with similar equilibrium temperatures of approximately 1400 K ([Blecic et al. 2014](#); [Zellem et al. 2014](#)). However, they orbit

* E-mail: katy.chubb@bristol.ac.uk

† E-mail: dominicsamra.uk@gmail.com

very different host stars: WASP-43 b orbits a K-type star every 0.813 days (Gillon et al. 2012), whilst HD 209458 b orbits a G0V star every 3.52 days (Torres et al. 2008). The planets also differ substantially in surface gravity with HD 209458 b having $\log_{10}(g [\text{cms}^{-2}]) = 2.9$, whereas WASP-43 b has a surface gravity closer to 4, as $\log_{10}(g [\text{cms}^{-2}]) = 3.7$ (Helling et al. 2021). HD 209458 b's and WASP-43 b's atmospheres have both been well studied theoretically as well as observationally. Helling et al. (2020) and Robbins-Blanch et al. (2022) both predict WASP-43 b to be cloudy based on global climate models (GCMs) combined with kinetic cloud models, with Robbins-Blanch et al. (2022) finding their cloudy models fit observed HST spectra better than clear ones. Barstow (2020) find evidence for clouds in the terminator region of HD 209458 b by analysing transmission spectra. Taylor & Parmentier (2023) analyse eclipse spectra of both WASP-43 b and HD 209458 b taking scattering properties of different materials used to form clouds into account. They find no evidence for dayside clouds on HD 209458 b but do expect dayside clouds on WASP-43 b. More recently, WASP-43 b has also been the subject of JWST MIRI phase curve observations by Bell et al. (2024) (as part of the JWST ERS program for transiting exoplanets - program ID: #1366), which has also shown strong evidence for clouds on the planet's nightside.

Fraine et al. (2021) infer a low geometric albedo, namely $A_g < 0.06$, for WASP-43b based on secondary eclipse observations using the Hubble Space Telescope's (HST) WFC3/UVIS instrument, observed between 0.2 - 0.8 μm . They compute model atmospheres that include various cloud species, and deduce a lack of reflective cloud species on the dayside of the planet in the pressure layers probed by eclipse observations (i.e. $P \leq 1$ bar), which yields WASP-43b's dark dayside. Blažek et al. (2022) also find a low geometric albedo for WASP-43b, namely $A_g < 0.16$, based on TESS observations in the optical, and Scandariato et al. (2022) find $A_g < 0.087$ using CHEOPS, TESS, and HST. The geometric albedo of HD 209458 b has also been observed to be low; using CHEOPS it was measured as 0.096 ± 0.016 by Brandeker et al. (2022). The authors find this low value of A_g to be consistent with a cloud-free atmosphere.

The presence and types of clouds in exoplanet atmospheres are an important component of exploring why these measured albedos are so low. The cloud materials thought to be important in hot giant exoplanet atmospheres can be predicted using global climate models (GCMs) post-processed with kinetic cloud models (e.g. Ackerman & Marley 2001; Helling et al. 2008a; Gao et al. 2020; Rooney et al. 2022; Helling et al. 2023). These predictions can be confirmed via observations, such as those of the 5 - 13 μm region via JWST's MIRI LRS instrument, which allow for observations of vibrational mode absorption features of cloud particles (Grant et al. 2023; Dyrek et al. 2024). Recent transmission observations by JWST, which probe the terminator regions of exoplanets, have yielded evidence for silicate cloud species in the atmospheres of hot Jupiter WASP-17b by Grant et al. (2023) (in the form of quartz, $\text{SiO}_2[\text{s}]$) and warm Neptune WASP-107b by Dyrek et al. (2024) (in the form of $\text{MgSiO}_3[\text{s}]$, $\text{SiO}_2[\text{s}]$ and $\text{SiO}[\text{s}]$). Albedo models and reflected light observations offer a complimentary technique which can further explore the nature of cloud species on the dayside of such exoplanets.

It is well known that the types of cloud particles in the atmospheres of these types of planets will influence their observed primary eclipse (transmission) and/or secondary eclipse (emission) spectra (Wakeford & Sing 2015; Pinhas & Madhusudhan 2017; Min et al. 2020; Ma et al. 2023; Taylor & Parmentier 2023), and their

albedos (Fraine et al. 2021; Barrientos et al. 2023; Chubb et al. 2023), through their absorption and scattering properties. Efforts are being made to progress knowledge on the properties of a large number of species predicted to be important in hot gaseous exoplanet atmospheres; investigating not only the distribution, size, and composition of clouds, but also the impact of fractal/irregularly versus spherically particle shapes on observed spectra (Adams et al. 2019; Dominik et al. 2021; Lodge et al. 2023), and of the porosity of the particles (Min et al. 2007; Samra et al. 2020; Ohno et al. 2020).

This paper is structured as follows. In Sect. 2, we first present the methods (Sect. 2.1) and results (Sect. 2.2) of atmospheric models of WASP-43 b and HD 209458 b which post-process GCM outputs with microphysical cloud formation models. We then use these results to compute geometric albedos of the same planets in Sect. 3, with methods outlined in Sect. 3.1 and the results in Sect. 3.2. We give our conclusions in Sect. 4.

2 ATMOSPHERIC MODELLING

2.1 Methods

We use a hierarchical modelling approach to cloud formation in the atmospheres of WASP-43 b and HD 209458 b, as has been used in Helling et al. (2021). We use 1D local temperatures, pressures and vertical wind speed profiles (T, p, v_z -profiles) from the cloud-free general circulation model (GCM) of ExpeRT/MITgcm (Carone et al. 2020; Baeyens et al. 2021) as input for our kinetic cloud formation model (Woitke & Helling 2003, 2004; Helling & Woitke 2006; Helling et al. 2008b). The ExpeRT/MITgcm is run for a simulation time of 1500 Earth days with solar metallicity, and the temperature, pressure and vertical velocity profiles are computed using the time-averages of their profiles over the last 100 days (Schneider et al. 2022).

In the case of WASP 43b, the ExpeRT/MITgcm used is the same as in Bell et al. (2024). For both planets, solar abundances are assumed for the GCM and for post-processing of the clouds, in the later case assuming Asplund et al. (2009) abundances. TiO and VO were taken out of the GCM computations for WASP-43 b in order to prevent a temperature inversion in the upper atmosphere, which Bell et al. (2024) found to be a better match to observed dayside emission and photometry. Previous GCM studies such as Kataria et al. (2015) have also taken out TiO and VO from their WASP-43 b models due to observations and analyses suggesting there is no temperature inversion (e.g. Blečić et al. 2014; Line et al. 2014). Suggestions of a temperature inversion in the atmosphere of HD 209458 b have previously been deduced by studies such as Burrows et al. (2007); Madhusudhan & Seager (2009), based on HST and Spitzer measurements available at the time. Slightly more recent observations and analyses conclude no evidence for a temperature inversion (Diamond-Lowe et al. 2014; Line et al. 2016), with more observations on the way from JWST to ideally provide more conclusive evidence. Similar GCMs of HD 209458 b to Schneider et al. (2022) such as Lee et al. (2021) also keep TiO and VO in, and therefore model a temperature inversion. As pointed out by Schneider et al. (2022) the dayside temperature of HD 209458 b is very close to the TiO and VO condensation curves (see e.g. Désert, J.-M. et al. 2008), which indicate their thermal stability, which is why it is not entirely obvious whether the species should be left in or out of the gas phase. Given this uncertainty, we chose to explore the theoretical impact of allowing TiO and VO and therefore a thermal

inversion in the atmosphere of HD 209458 b, but not WASP-43 b. This causes a difference in the outcomes of our models, allowing us to explore how subtle differences in the atmospheric chemistry of two planets with otherwise similar effective temperatures can impact observed planetary properties such as albedo. The other main difference between the two planets is that the atmosphere of HD-209458 b is more inflated than that of WASP-43 b (Schneider et al. 2022). In total, 120 1D profiles were extracted from the GCM, spaced at 15 degrees in longitude, and every 22.5 degrees in latitude. An additional ‘polar latitude’ of 86° was also included. The full spatial resolution is used for the mapping of the model clouds, but only a select number of regions are used for computing the dayside albedo (see Sect. 3.1).

With the approach of using the output of GCMs as input to our kinetic cloud model, we are able to consider a set of 16 condensates (TiO₂[s], SiO[s], SiO₂[s], MgO[s], MgSiO₃[s], Mg₂SiO₄[s], Fe₂SiO₄[s], Fe[s], Fe₂O₃[s], FeO[s], FeS[s], KCl[s], NaCl[s], Al₂O₃[s], CaSiO₃[s], CaTiO₃[s]) simultaneously, which consistently condense as mixed-composition (heterogeneous) cloud particles. *Condensation* is considered kinetically through a set of 132 reactions. To start the process of cloud formation, cloud condensation nuclei are formed through *nucleation*, treated through modified classical nucleation theory (Lee et al. 2018), for 4 species (TiO₂[s], SiO[s], KCl[s], NaCl[s]). *Gravitational settling* of cloud particles occurs according to the size of the cloud particles assuming equilibrium drift velocities (Woitke & Helling 2003).

Cloud formation is coupled to the gas-phase through *element depletion*, the gas-phase is then solved for using the chemical equilibrium code GGChem (Woitke et al. 2018). *Element replenishment* is treated using a relaxation timescale approach, local elemental abundances return towards the initial elemental abundances considering mixing from the deep atmosphere on a given timescale (see Eqs. 6 and 7 in Woitke & Helling (2004)). The mixing timescale is computed from the vertical velocity component of the GCM using the standard-deviation of vertically adjacent cells from the GCM solution, as described in Appendix B in Helling et al. (2023). Following Samra et al. (2023), we use this mixing timescale increased by a factor of 100. This has been found to more appropriately reflect the efficiency of mixing and better reproduce observations of cloud optical depth for WASP 96b and WASP 39b (Samra et al. 2023; Espinoza et al. 2024). Furthermore, GCM studies find a similar relationship between the root-mean squared velocity times the pressure scale height, and the eddy diffusion coefficient for (K_{zz}) for passive tracer hazes and cloud particles (Steinrueck et al. 2021; Parmentier et al. 2013).

In order to compute the geometric albedo A_g of a cloudy planet, a particle size distribution is required. The kinetic cloud formation model used treats the cloud particle population through the series of moments ($\rho L_j = \int_{V_l}^{\infty} V^j f(V) dV$), so the size distribution ($f(V)$) is not explicitly known. However a particle size distribution that is consistent with the moments can be re-constructed, providing a functional form with suitably few parameters (Helling et al. 2008b). In this work we derive the parameters for a log-normal distribution motivated by its common use in modelling cloud particle size distributions in exoplanet atmosphere models (Ackerman & Marley 2001; Wakeford & Sing 2015; Mai & Line 2019; Roman & Rauscher 2019; Mukherjee et al. 2021, e.g.). The derivation of the parameters can be found in Appendix A.

2.2 Results

There is quite a difference between the pressure-temperature profiles of the two planets (seen in Fig. 1), with the region around the substellar point of HD 209458 b exhibiting a temperature inversion, due to the inclusion of TiO and VO in the GCM of HD 209458 b but not WASP-43 b (see discussion at the start of Sect. 2.1). As a consequence of these high temperatures, clouds do not form in the upper atmosphere (at pressures below ~ 0.01 bar) around this region of HD 209458 b. In contrast, our models predict WASP-43b to be relatively cloudy throughout the dayside and down to low pressures, due to the relatively cooler upper-atmosphere temperatures. Fig. 2 shows the composition V_s of the cloud particles used in this work as fractions of the total cloud particle volume V_{tot} , for the substellar regions on WASP-43 b (upper) and HD 209458 b (lower). The cloud particles are substantially mixed at all pressures, with the most abundant cloud species not exceeding 60%. For the bulk of the cloud deck at the substellar point on both planets, the dominant cloud condensate is either Mg₂SiO₄[s] or MgSiO₃[s], and Fe[s] (the most abundant iron-bearing condensate) does not exceed around 20%, except at the base of the cloud deck where silicate material evaporates.

Figure 3 shows the derived log-normal size distributions for cloud particles at individual pressure levels throughout the atmosphere for both planets. In the case that the distribution becomes monodisperse (i.e. no valid solution for the log-normal parameters exists), only the average particle size is shown. The average particle size derived from the moments, i.e. $\langle a \rangle = (3/4\pi)^{1/3} L_1/L_0$, is shown in dashed green, with a good agreement between the log-normal average particle size at all pressures. Also shown are the nucleation rates, showing the broadness of the size distribution in regions with efficient nucleation: there is a significant population of small cloud particles resulting from ‘recently nucleated’ particles that have not yet undergone substantial particle growth. In the deeper parts of the cloud deck, the cloud particle size distribution is close to monodisperse, because there nucleation has ceased to be an efficient process. Hence, the only processes that affect the particle size distribution are bulk growth/evaporation, or settling. As bulk growth is very efficient, the particles quickly grow to the maximum size for their pressure level to then rain out rapidly. Thus the only stable particle size distribution possible is close to monodisperse around this - large - particle size. See Woitke & Helling (2003) for a discussion of the maximum particle size when considering equilibrium velocity rain-out of cloud particles.

As our aim is to investigate the dayside geometric albedo, it is also instructive to look at isobaric maps of various cloud properties for the dayside of these exoplanets. Isobaric maps are shown for WASP 43 b and HD 209458 b at 10 mbar in Figs. 4 and 5, respectively. The grey regions indicate where there are no cloud particles. Additional maps at other pressure levels can be found in Figs. B1 - B4. The effect of the temperature inversion at the substellar point is also nicely seen in maps of the cloud formation results, which is in particular evident in Fig. B4 as almost the entire dayside of HD 209458 b is devoid of cloud formation at that pressure level of 1 mbar (the grey area).

Where the temperature is higher, silicate materials are less thermally stable than iron-bearing oxides, metallic iron and iron sulphide, hence the volume fraction of iron bearing species increases, this coincides with a reduction in cloud particle mass load (ρ_d/ρ). For example this is illustrated nicely for WASP-43 b in Fig. 4, comparing the top left and right plots, and the bottom right plot. This is more difficult to see for HD 209458 b at 10 mbar in

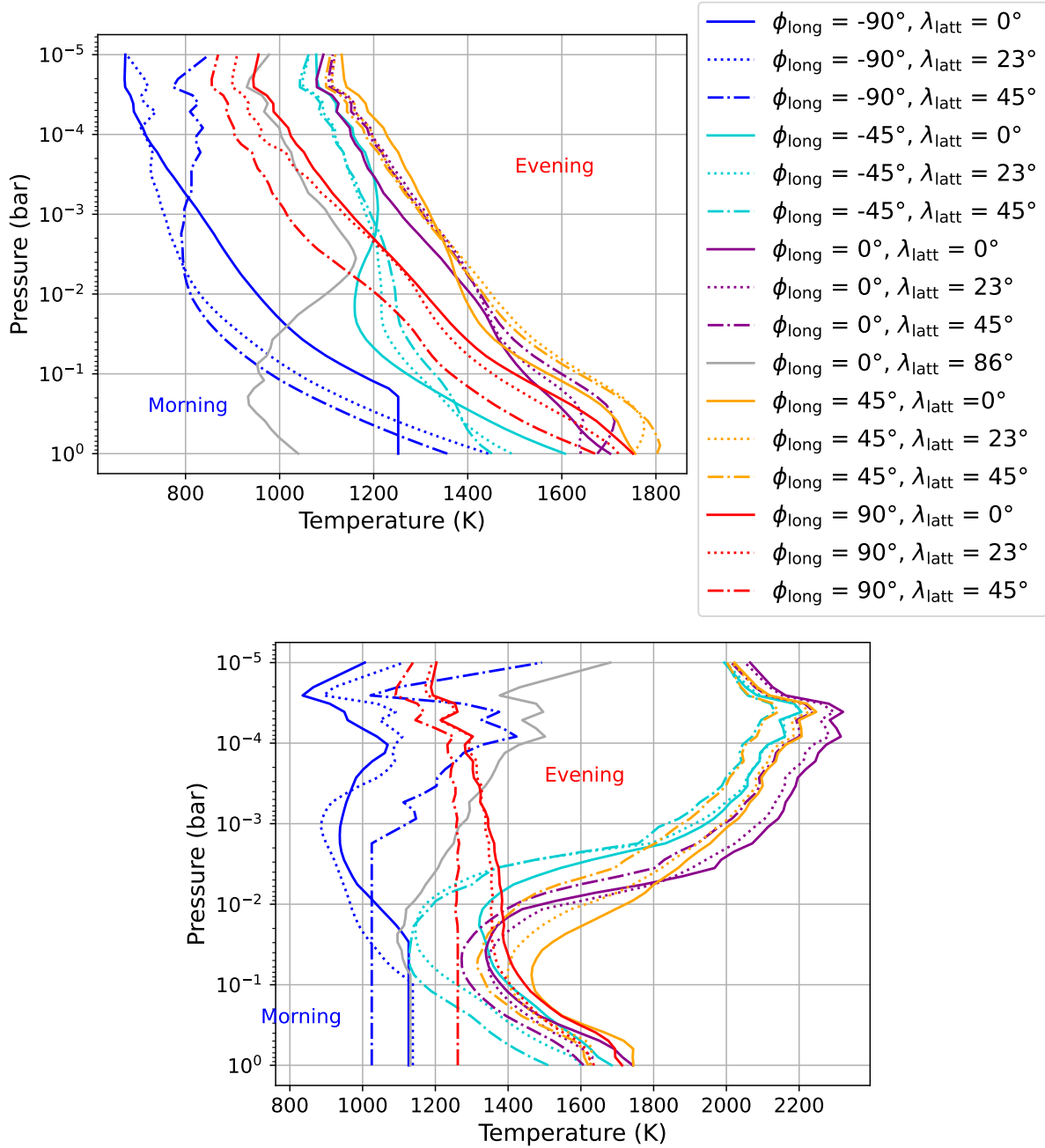


Figure 1. Pressure-temperature profiles for the various longitude-latitude regions across WASP-43 b (upper) and HD 209458 b (lower).

Fig. 5 because of the absence of cloud material at the hot-spot on the dayside.

The grey regions indicate where there is no cloud material: for particular quantities (number density n_d , and average particle size $\langle a \rangle$) there is no data across these regions. For quantities that are only meaningful to discuss above a certain limit, but their values nonetheless remain non-zero, extended colour-bar minimums are used. For example, we truncate the colour maps for all nucleation rates at $J_{\text{tot}} = 10^{-20} [\text{cm}^{-3}\text{s}^{-1}]$. This is equivalent to approximately one new particle per cm^3 every 1000 current universe lifetimes, a very conservative lower limit for meaningful nucleation. Hence any nucleation rate values below this limit are shown as part of the last colour level. The reason for the sudden drop-off in nucleation rate

seen in the maps (Figs. 4 - 5), is because when nucleation becomes thermally unfavourable it tends to reduce rapidly (see Fig. 3).

3 GEOMETRIC ALBEDO MODELLING

3.1 Methods

The geometric albedo A_g of a transiting exoplanet is a property that can be inferred by observing the star and the planet just before/after and during the planet's secondary eclipse. It is defined as the ratio of reflected flux at $\alpha = 0^\circ$, when the planet is directly behind the host star as seen by an observer, compared to a Lambertian (i.e. white and isotropically reflecting) flat disk of the same cross-sectional

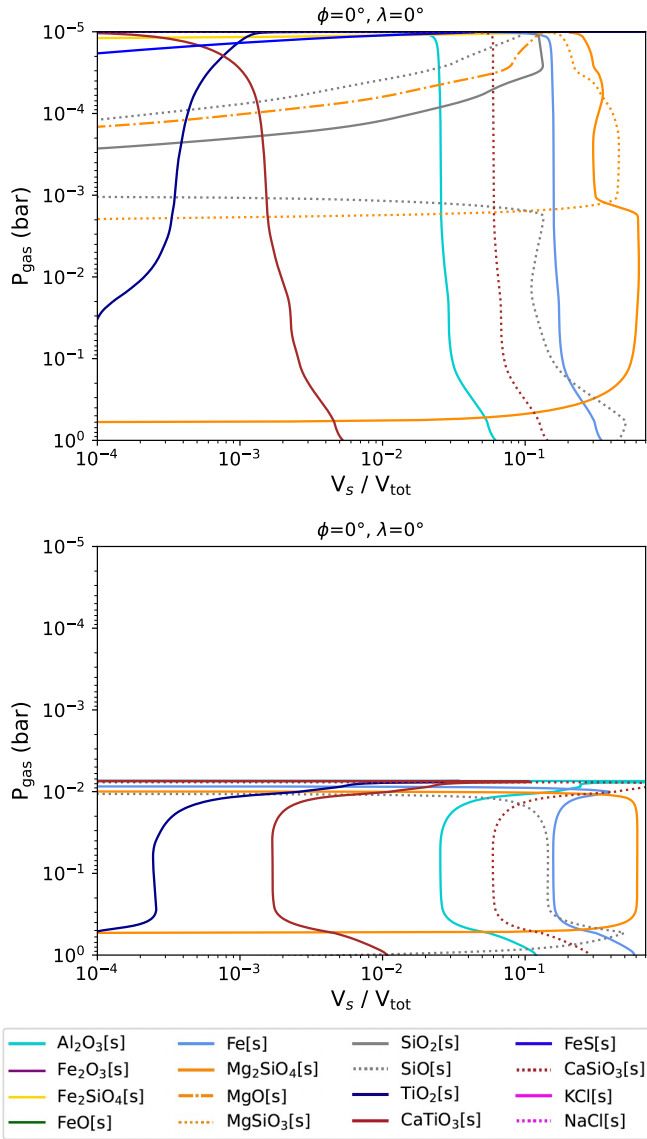


Figure 2. Composition V_s of the cloud particles used in this work as fractions of the total cloud particle volume V_{tot} , for the substellar regions on WASP-43 b (upper) and HD 209458 b (lower).

area. For gaseous exoplanets of the temperatures considered in this paper, we expect reflected light to dominate in the visible and UV where thermal emission is negligible, before thermal emission starts to dominate in the infrared. Instruments such as CHEOPS therefore cover the reflected light dominated part of the spectra.

In this work we use the Polarisation of Hot Exoplanets (PolHEX) code (Chubb et al. 2023) to simulate the flux that is reflected by the model atmospheres of hot gas giant exoplanets HD 209458 b and WASP-43 b, as described in Sect. 2.2. PolHEX is based on the adding-doubling radiative transfer algorithm of de Haan et al. (1987), adapted for modelling polarised reflected light spectra of exoplanets by Stam et al. (2006); Stam (2008), and recently further adapted for inhomogeneous transiting exoplanets by Chubb et al. (2023). Multiple scattering effects are fully included in the radiative transfer part of the code (de Haan et al. 1987). We use a planetary scattering matrix for the model atmosphere which is normalised on the planet’s geometric albedo A_g when the reflected flux is inte-

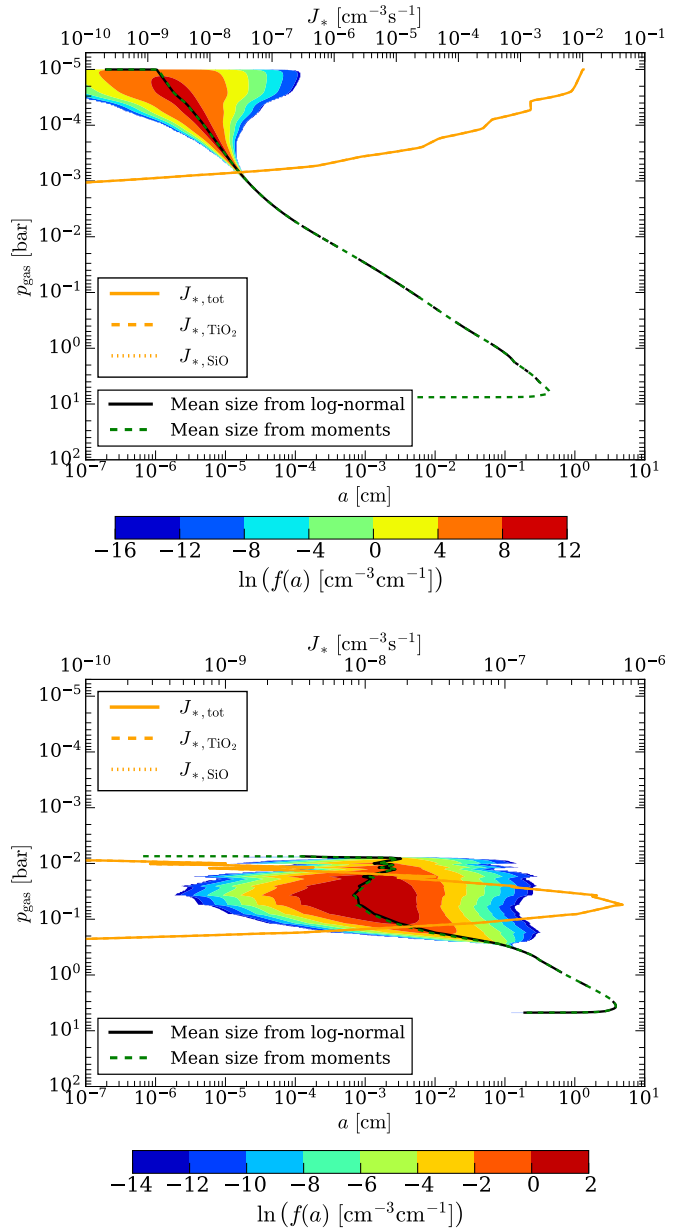


Figure 3. Log-normal cloud particle size distribution for the substellar regions on WASP-43 b (upper) and HD209458 b (lower). The cloud particle size distribution is shown as filled contours. The average particle size from the log-normal distribution is shown as the black solid line. The average particle size derived from the moments is shown as the dashed green line. The orange lines indicate the nucleation rates.

grated over the visible part of the planet at a phase angle of $\alpha = 0^\circ$, i.e. when a transiting planet is directly behind the star from the point of view of the observer. We compute A_g as a function of the wavelength, and integrate over the CHEOPS bandpass (0.35 - 1.1 μm) in order to be able to compare simulations against observations of WASP-43 b and HD 209458 b.

It has been shown that errors of several percent can be introduced into computations of the geometric albedo when the linear polarisation state of light is not taken into account (Stam & Hovenier 2005) because the polarisation state influences the scattering processes. We therefore use a 3×3 matrix to compute the reflected flux and the geometric albedo. See Chubb et al. (2023) for details.

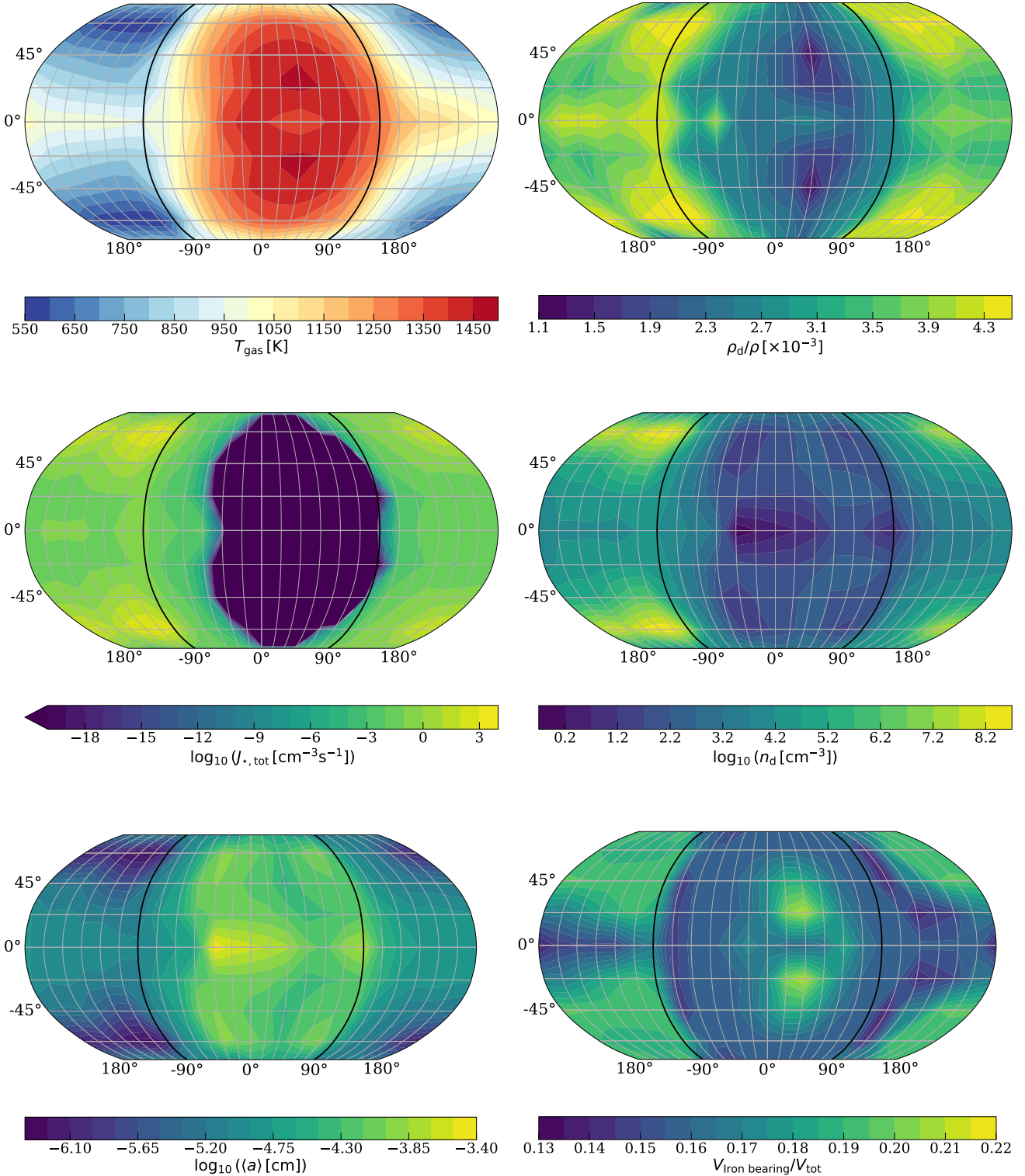


Figure 4. GCM and cloud formation results for WASP-43 b at $p_{\text{gas}} = 10$ mbar. The maps are centred on the substellar point ($\phi_{\text{long}} = 0^\circ$, $\lambda_{\text{lat}} = 0^\circ$), with the terminator limbs ($\phi_{\text{long}} = \pm 90^\circ$) shown in bold black lines. **Top Left:** The local gas temperature from the GCM solution. **Top Right:** Cloud particle mass load in the atmosphere as the ratio of the density of cloud particle mass to the gas density. **Middle Left:** Total nucleation rate. **Middle Right:** Cloud particle number density. **Bottom Left:** Average cloud particle size. **Bottom Right:** Volume fraction of the cloud particles composed of iron-bearing condensate species. The iron-bearing condensates volume fraction is the sum of the volume fractions for Fe[s], FeS[s], FeO[s], Fe₂O₃[s], Fe₂SiO₄[s].

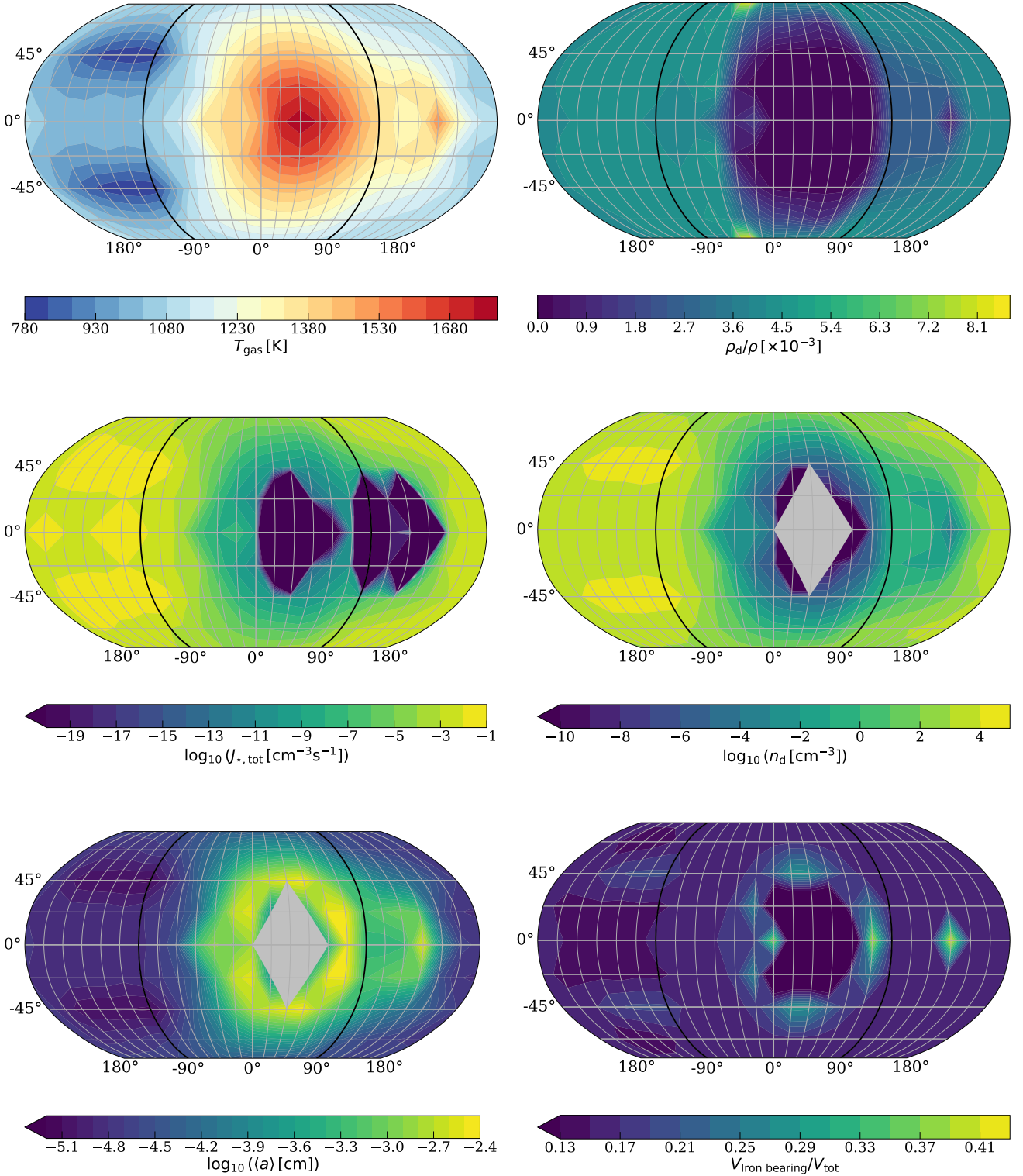


Figure 5. GCM and cloud formation results for HD 209458 b at $p_{\text{gas}} = 10$ mbar. The maps are centred on the substellar point ($\phi_{\text{long}} = 0^\circ$, $\lambda_{\text{lat}} = 0^\circ$), with the terminator limbs ($\phi_{\text{long}} = \pm 90^\circ$) shown in bold black lines. **Top Left:** The local gas temperature from the GCM solution. **Top Right:** Cloud particle mass load in the atmosphere as the ratio of the density of cloud particle mass to the gas density. **Middle Left:** Total nucleation rate. **Middle Right:** Cloud particle number density. **Bottom Left:** Average cloud particle size. **Bottom Right:** Volume fraction of the cloud particles composed of iron-bearing condensate species.

Figure 1 gives the pressure-temperature profiles of the different atmospheric regions as computed using the GCM and kinetic cloud models. We chose to model the reflection (geometric albedo) spectra using the regions represented by solid lines in these figures only, as it can be seen that the latitudinal variation is not as strong as the longitudinal variation. As a consequence of the higher temperatures in the upper atmosphere of HD 209458 b, due to the inclusion of TiO and VO in the GCM, clouds do not form in the upper atmosphere (at pressures below ~ 0.01 bar) around this region of HD 209458 b. In contrast, our models predict WASP-43b to be relatively cloudy throughout the dayside and up to low pressures, due to the relatively cooler upper-atmosphere temperatures, with no TiO and VO included in those GCMs (Bell et al. 2024).

For the different cloud species predicted by the kinetic cloud models of the two planets, we combine the refractive indices together for each cloud layer to form inhomogeneous clouds using effective medium theory (e.g. Mishchenko et al. 2016). The refractive indices of individual materials that we assume are given in Table 1. The material volume fractions V_s / V_{tot} of the different materials forming the mixed-material cloud particles as a function of pressure are illustrated in Fig. B5 for WASP-43 b and Fig. B6 for HD 209458 b, for the longitude and latitude regions used in this work. It can be seen that while WASP-43 b is expected to retain clouds up to high altitudes across the dayside, the clouds are limited to higher pressure layers, > 0.01 bar, around the hotspot region of HD 209458 b according to our model atmospheres. We do not include refractive indices for NaCl or KCl in Table 1 as these do not contribute to the material volume fractions of either of our target planets. The only refractive index data we could find for CaTiO₃ (perovskite) is from Posch et al. (2003), but it is only available at wavelengths greater than $2 \mu\text{m}$ which is higher than we need for this study, so we also do not use it here.

The most abundant gas-phase molecular and atomic species for the sub-stellar point for the two planets are shown in Fig. 6 (left) for WASP-43 b and Fig. 6 (right) for HD 209458 b. We include the species shown in our models at the volume mixing ratios (VMRs) specified, using opacities which were computed for constructing the ExoMolOP database (Chubb et al. 2021), and line lists for each species as follows. H₂O (Polyansky et al. 2018), CO (Li et al. 2015), HCl (Gordon et al. 2022), H₂S (Azzam et al. 2016), SiS (Upadhyay et al. 2018), SiO (Yurchenko et al. 2021), Na (Allard et al. 2019; Kurucz & Bell 1995), K (Allard et al. 2016; Kurucz & Bell 1995), TiO (McKemmish et al. 2019), SH (Yurchenko et al. 2018), CO₂ (Yurchenko et al. 2020), CH₄ (Yurchenko et al. 2017), VO (McKemmish et al. 2016). We note that the VMR of VO lies just below the lower limit of the x-axis of Fig. 6 (right), at approximately 3×10^{-9} throughout the atmosphere.

For planets that orbit very close to their host star, such that the planet-star distance is not much greater than the planetary radius, it is no longer a good approximation to consider incident starlight to be parallel. We follow the methods of Palmer (2019) and introduce a stellar grid to represent the contribution from different regions of the star to each planetary grid point, and include the planet-star distance, stellar radius and planetary radius into our computations. We compute limb darkening using the quadratic law (Kopal 1950; Howarth 2011) with coefficients of $a = 0.67679$, $b = 0.07477$ for WASP-43 and $a = 0.44756$, $b = 0.27543$ for HD 209458 taken from Table 2 of Claret (2021). In Fig. B7, we demonstrate the difference made by implementing the stellar grid and limb darkening effects to the close-in model exoplanet atmosphere of WASP-43b, by plotting the reflected flux F at $\lambda = 0.35 \mu\text{m}$ as a function of the planetary phase angle α . The differences are largest at $\alpha = 0^\circ$, the phase angle

that we are focused on in this study, showing the importance of accounting for the non-parallel incident light.

3.2 Results

Figure 7 shows the main results of our study: the geometric albedo A_g computed wavelength-dependent and integrated over the CHEOPS bandpass for WASP-43 b and HD 209458 b. The ‘transmitted geometric albedo’ refers to the geometric albedo weighted by the CHEOPS filter throughput function and the CCD sensitivity, as taken from <http://svo2.cab.inta-csic.es/theory/fps/>. Although the pressure-temperature profiles of the atmospheres show marked differences (Fig. 1), resulting in different levels of cloudiness across the daysides, our models predict both planets to exhibit relatively similar geometric albedos across the CHEOPS bandpass. The geometric albedos of WASP-43b and HD 209458 b as observed by CHEOPS alone are only ~ 0.14 (Scandariato et al. 2022)¹ and 0.096 ± 0.016 (Brandeker et al. 2022), respectively. If we compare our model results to these by computing over the CHEOPS bandpass, we find 0.026 (compared to ~ 0.14) for WASP-43 b and 0.028 (compared to 0.096 ± 0.016) for HD 209458 b. Figure 8 shows the wavelength-dependent geometric albedos for each of the atmospheric regions we included in our models, along with the horizontally inhomogeneous atmospheres for comparison, for WASP-43 b and HD 209458 b.

It is interesting to see in Fig. 8 that the high-latitude region ($\lambda_{\text{lat}} = 86^\circ$) of HD 209458 b has a much larger albedo than the equatorial region. This is due to the higher proportion of reflective materials as compared to Fe-bearing species in this region’s upper atmospheric clouds; see Fig. B6. The reason for this can be seen in Fig. 1: qualitatively, the pressure-temperature structure of the high-latitude region is similar to that of the morning terminator. However, it is hotter overall due to it being on the dayside. Comparing the pressure-temperature structure of the high-latitude region with Fig. 14 in Helling et al. (2021) (which shows Solar-abundance supersaturation curves), it is clear that the temperature inversion for the high-latitude region exceeds 1400 K at $\sim 10^{-4}$ bar. For this upper part of the high-latitude region atmospheres, the temperature is above the thermal stability for all the condensates except TiO₂[s], Al₂O₃[s], CaTiO₃[s] and CaSiO₃[s]. Crucially, this does not include any of the Fe-bearing species necessary for dark clouds. However, the temperatures in the upper atmosphere are still low enough for cloud formation to occur, through TiO₂[s] nucleation at low pressures (until above 9×10^{-4} bar).

It can be seen in Fig. 9 that models using the same input parameters for both WASP-43b (left) and HD 209458 b (right) but leaving out strongly absorbing Fe-bearing species such as Fe[s], FeO[s], FeS[s], and Fe₂O₃[s] in forming the cloud layers yield a much higher geometric albedo than when all species are included. Although Fe₂SiO₄[s] is also an Fe-bearing species, it does not have the same strongly absorbing properties as the others mentioned, and behaves more like a reflecting silicate. In the case of HD 209458 b, A_g can reach very high in the instance that we remove the Fe-bearing species, due to the lack of absorbing clouds high in the atmosphere and the now highly-reflective clouds further down. Strong molecular and atomic absorption features can be seen due to the clear upper atmosphere.

In general, our predicted geometric albedos from GCM and kinetic cloud model predictions are slightly lower than those inferred

¹ estimated based on parameters and figures provided in the paper

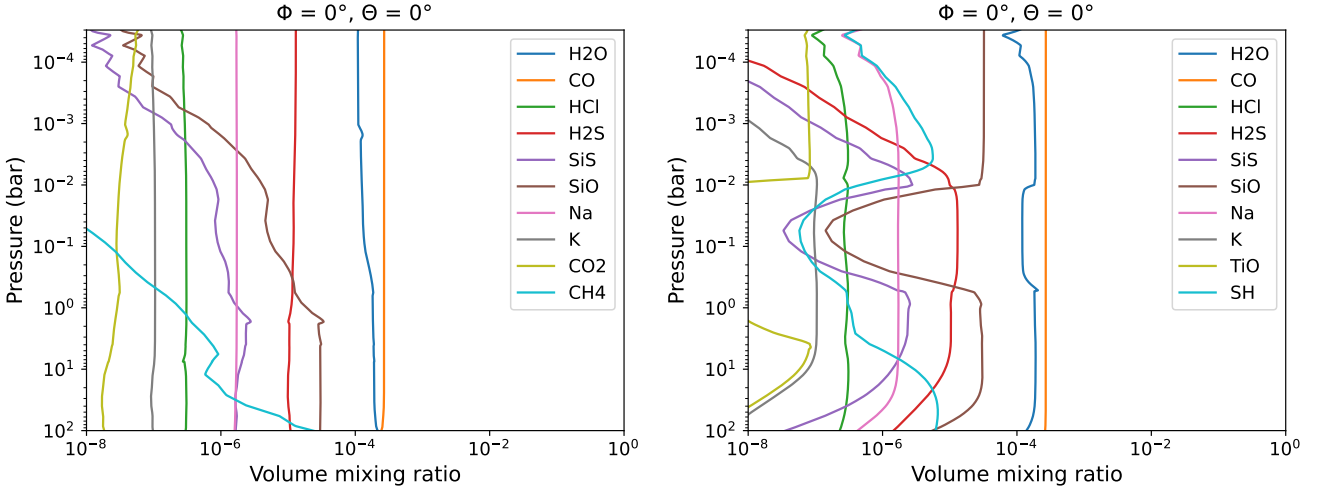


Figure 6. Volume mixing ratios (VMRs) of the most abundant gas-phase molecular and atomic species at the sub-stellar points of WASP-43 b (left) and HD 209458 b (right), based on our model atmospheres. **The VMR of VO is approximately 3×10^{-9} throughout the atmospheres and is thus not visible in these plots.**

Species	Name	Source
Al ₂ O ₃ [s] (crystalline)	Corundum	Palik (2012)
CaSiO ₃ [s] (crystalline)	Wollastonite	He (2013)
Fe ₂ O ₃ [s] (solid)	Hematite	Triaud (2005) ^a
Fe ₂ SiO ₄ [s] (crystalline)	Fayalite	Unpublished ^b
FeO[s] (amorphous)	Wustite	Henning et al. (1995)
FeS[s] (crystalline)	Troilite	Pollack et al. (1994)
Fe[s] (metallic)	Iron	Palik (2012)
Mg ₂ SiO ₄ [s] (amorphous)	Forsterite	Jäger et al. (2003)
MgO[s] (cubic)	Magnesium oxide	Palik (2012)
MgSiO ₃ [s] (amorphous)	Enstatite	Dorschner et al. (1995)
SiO ₂ [s] (crystalline)	Quartz	Palik (2012)
SiO[s] (non-crystalline)	Silicon oxide	Palik (2012)
TiO ₂ [s] (rutile)	Rutile	Zeidler et al. (2011)

Table 1. Sources used for the real (n) and imaginary (k) parts of the refractive indices of the species that form the cloud particles in this work. All species are in the solid phase, indicated by [s].

^a Downloaded via the Aerosol Refractive Index Archive (ARIA) at <http://eodg.atm.ox.ac.uk/ARIA/>

^b Accessed via the Database of Optical Constants for Cosmic Dust at <https://www.astro.uni-jena.de/Laboratory/OCDB/crsilicates.html>

from observations. We might expect that an atmosphere which has a slightly lower proportion of Fe-bearing species than assumed by us to match the observed data better. The reduced albedo features just under 0.6 and 0.8 μm in Fig. 9 are due to the strongly absorbing Na and K doublets.

4 CONCLUSION

Based on our model atmospheres and using a radiative transfer code that fully includes multiple scattering, polarization and non-parallel incident starlight, we find geometric albedos A_g of 0.026 for WASP-43b and 0.028 for HD 209458 b in the CHEOPS band-pass, which compare to $A_g \sim 0.14$ (Scandariato et al. 2022) and 0.096 ± 0.016 (Brandeker et al. 2022) measured geometric albedos

for these planets, respectively. We compare to a model atmosphere which does not contain any Fe-bearing species to demonstrate the dramatic impact these particles have on the albedo. We find that A_g increases from 0.024 to 0.518 when no strongly absorbing Fe-bearing species are included in our WASP-43b model atmosphere, and from 0.021 (with Fe-bearing species) to 1.37 (without Fe-bearing species) for HD 209458 b.

Our models predict Fe-bearing species to be abundant enough in these atmospheres to reduce A_g to a value consistent with, or lower than, observations, in contrast to highly reflective clouds formed from silicate species alone. We predict that these atmospheres contain a combination of cloud species whose combined scattering and absorption properties lead to a relatively low observed albedo. We demonstrate that the contribution of Fe-bearing species to cloud particles, even at relatively small abundances, can

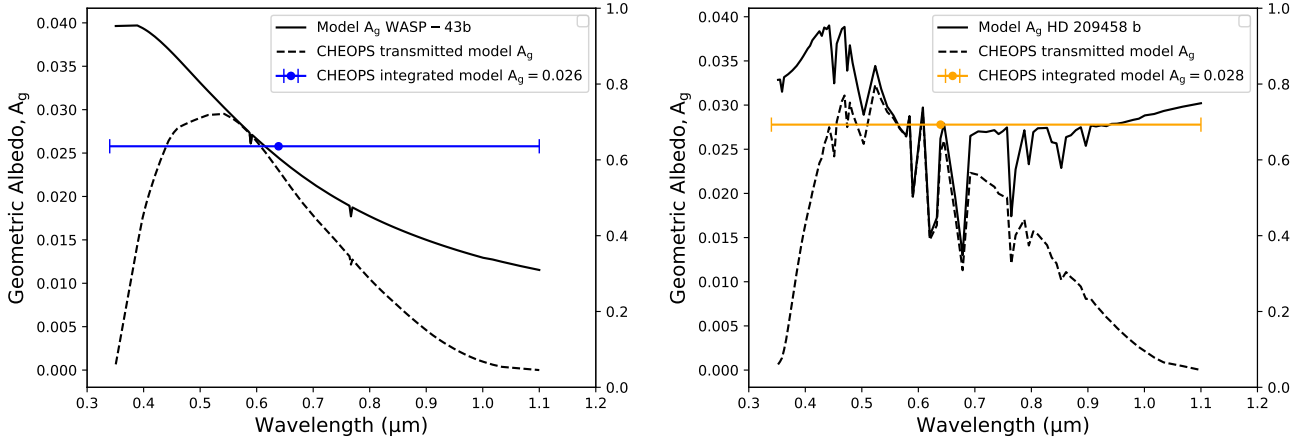


Figure 7. Geometric albedos A_g of WASP-43 b (left) and HD 209458 b (right) for our model horizontally inhomogeneous atmospheres, and integrated over the CHEOPS bandpass. Here ‘transmitted geometric albedo’ is the signal multiplied by the CHEOPS filter throughput function and CCD sensitivity curve (transmission fraction).

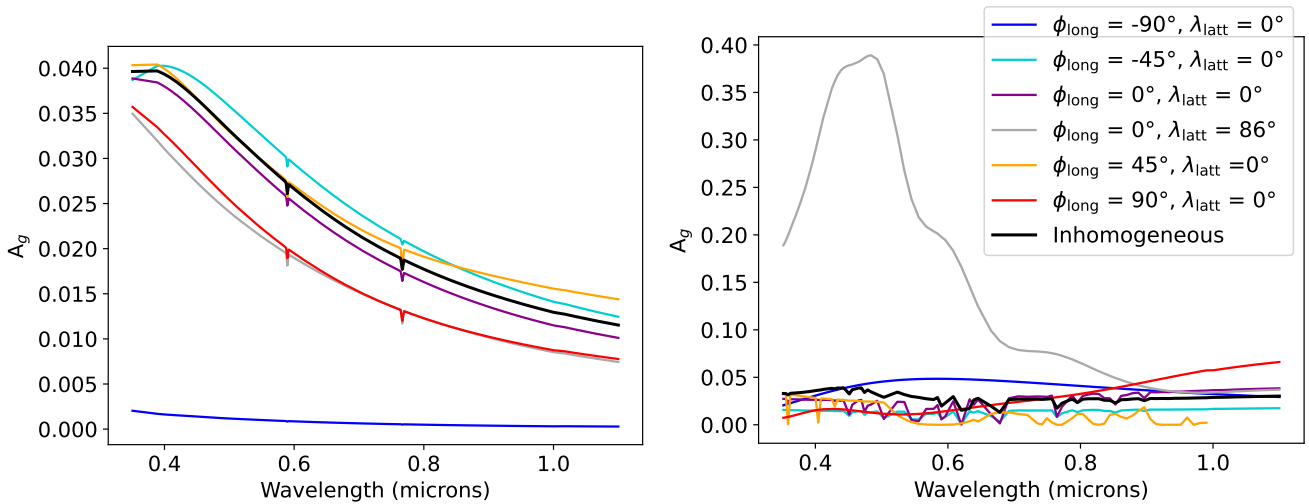


Figure 8. Geometric albedos A_g of WASP-43 b (left) and HD 209458 b (right) for selected atmospheric regions, and (in black) a combination of the shown regions for the assumption of a mainly horizontally inhomogeneous atmosphere.

reduce the overall geometric albedo to the same extent as a clear atmosphere.

It is important to note that our model predictions must also match observed transmission (primary eclipse) and emission (secondary eclipse) spectra of exoplanets, which typically do not provide evidence for very dense cloud cover. As discussed in [Samra et al. \(2023\)](#), there are various mechanisms which can explain an atmosphere which is relatively cloudy but still transparent enough that clear molecular and atomic signatures can be seen; for example, increased atmospheric mixing or increased porosity of cloud particles. It would be of interest to explore further the impact of other cloud properties such as different particle size distributions or cloud particles with a fractal nature (see, e.g., [Lodge et al. 2023](#)) on the computed geometric albedo. The assumptions and choices made throughout our models, such as including TiO and VO in the GCM of HD 209458 b but not in that of WASP-43b (see discussion at the start of Sect. 2.1), have an impact on our results which may not be indicative of the true nature of the planetary atmospheres.

We do, however, demonstrate how these different choices impact our final models, and find that despite these differences, both our model atmospheres yield relatively low geometric albedos, largely due to the impact that including Fe-bearing species in the formation of clouds has on the atmospheres.

We conclude that the geometric albedo alone cannot be used as conclusive evidence for a clear dayside, particularly for the types of exoplanet explored in this study, and must be used in combination with other observational techniques in order to deduce the most likely nature of the atmosphere. We stress that albedo models should be used in combination with other spectra derived observational techniques, such as transmission ([Grant et al. 2023](#); [Dyrek et al. 2024](#)), emission ([Taylor & Parmentier 2023](#)), or even polarised reflection spectra ([Bailey et al. 2018](#); [Chubb et al. 2023](#)), to gain the maximum amount of information possible about the cloud particles in these exotic exoplanet atmospheres.

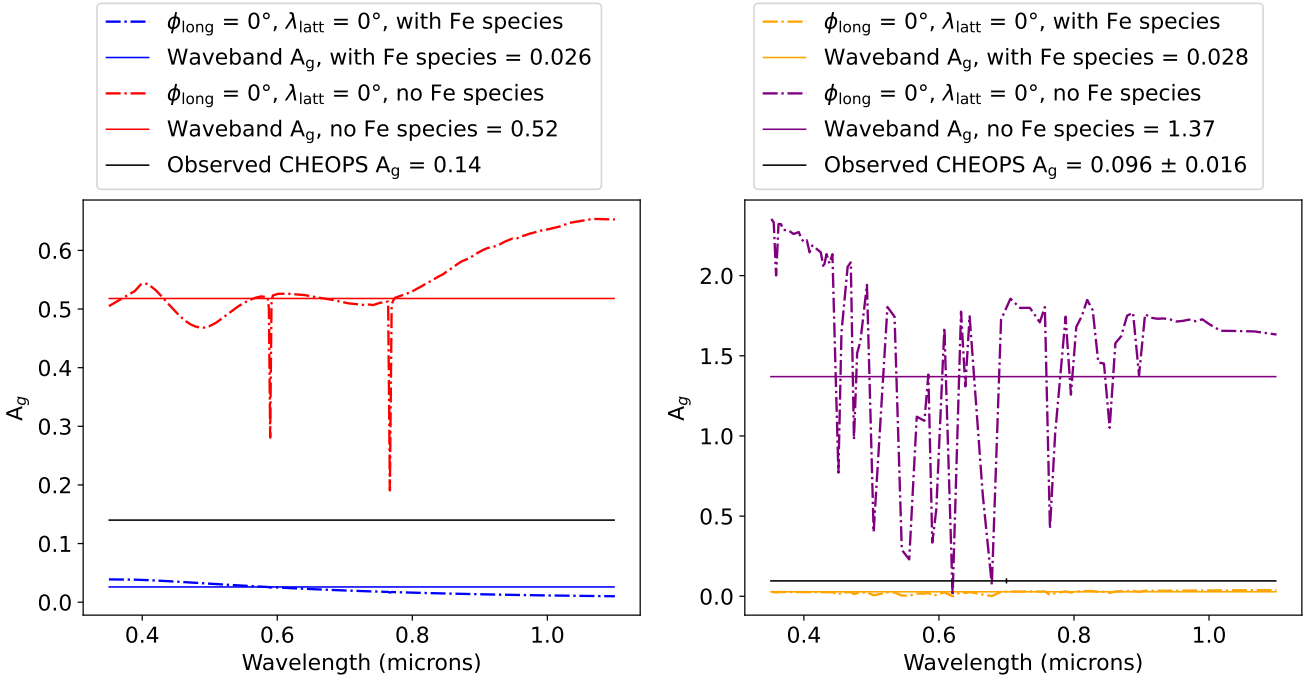


Figure 9. Geometric albedos A_g of WASP-43 b (left) and HD 209458 b (right) for an atmospheric region on the middle of the planetary disk, comparing with and without including Fe-bearing species. Values of A_g integrated over the CHEOPS bandpass for our model atmospheres are also shown, along with values deduced from CHEOPS observations of $A_g \sim 0.14$ (WASP-43 b) (Scandariato et al. 2022) and 0.096 ± 0.016 (HD 209458 b) (Brandeker et al. 2022).

ACKNOWLEDGEMENTS

This project has received funding from STFC, under project number ST/V000861/1. Ch.H. and L.C. acknowledges funding from the European Union H2020-MSCA-ITN-2019 under grant agreement no. 860470 (CHAMELEON). D.S. acknowledges financial support and use of the computational facilities of the Space Research Institute of the Austrian Academy of Sciences. K.L.C further acknowledges funding by UK Research and Innovation (UKRI) under the UK government’s Horizon Europe funding guarantee as part of an ERC Starter Grant [grant number EP/Y006313/1].

DATA AVAILABILITY

The data underlying this article will be shared on reasonable request to the corresponding author(s).

REFERENCES

- Ackerman A. S., Marley M. S., 2001, *ApJ*, 556, 872
 Adams D., Gao P., de Pater I., Morley C. V., 2019, *ApJ*, 874, 61
 Allard N. F., Spiegelman F., Kielkopf J. F., 2016, *A&A*, 589, A21
 Allard N. F., Spiegelman F., Leininger T., Mollière P., 2019, *A&A*, 628, A120
 Angerhausen D., DeLarme E., Morse J. A., 2015, *Publications of the Astronomical Society of the Pacific*, 127, 1113
 Asplund M., Grevesse N., Sauval A. J., Scott P., 2009, *ARA&A*, 47, 481
 Azzam A. A. A., Yurchenko S. N., Tennyson J., Naumenko O. V., 2016, *Mon. Not. R. Astron. Soc.*, 460, 4063
 Baeyens R., Decin L., Carone L., Venot O., Agúndez M., Mollière P., 2021, *Mon. Not. R. Astron. Soc.*, 505, 5603
 Bailey J., Kedziora-Chudczer L., Bott K., 2018, *Mon. Not. R. Astron. Soc.*, 480, 1613
 Barrientos J. G., MacDonald R. J., Lewis N. K., Kaltenegger L., 2023, *ApJ*, 946, 96
 Barstow J. K., 2020, *Mon. Not. R. Astron. Soc.*, 497, 4183
 Bell T. J., et al., 2024, *arXiv e-prints*, p. arXiv:2401.13027
 Blažek M., et al., 2022, *Mon. Not. R. Astron. Soc.*, 513, 3444
 Blečić J., et al., 2014, *ApJ*, 781, 116
 Brandeker A., et al., 2022, *A&A*, 659, L4
 Burrows A., Hubeny I., Budaj J., Knutson H. A., Charbonneau D., 2007, *ApJ*, 668, L171
 Carone L., et al., 2020, *Mon. Not. R. Astron. Soc.*, 496, 3582
 Charbonneau D., Brown T. M., Latham D. W., Mayor M., 2000, *ApJL*, 529, L45
 Chubb K. L., et al., 2021, *A&A*, 646
 Chubb K. L., Stam D. M., Helling C., Samra D., Carone L., 2023, *Mon. Not. R. Astron. Soc.*, 527, 4955
 Claret A., 2021, *Research Notes of the AAS*, 5, 13
 Désert, J.-M. Vidal-Madjar, A. Lecavelier des Etangs, A. Sing, D. Ehrenreich, D. Hébrard, G. Ferlet, R. 2008, *A&A*, 492, 585
 Diamond-Lowe H., Stevenson K. B., Bean J. L., Line M. R., Fortney J. J., 2014, *ApJ*, 796, 66
 Dominik C., Min M., Tazaki R., 2021, OpTool: Command-line driven tool for creating complex dust opacities, *Astrophysics Source Code Library*, record ascl:2104.010
 Dorschner J., Begemann B., Henning T., Jaeger C., Mutschke H., 1995, *A&A*, 300, 503
 Dyrek A., Min M., Decin L., Bouwman J., et al., 2024, *Nature*, 625, 51
 Espinoza N., et al., 2024, *Nature*
 Esteves L. J., De Mooij E. J., Jayawardhana R., 2015, *ApJ*, 804, 150
 Evans T. M., et al., 2013, *ApJ*, 772, L16
 Fraire J., et al., 2021, *AJ*, 161, 269
 Gao P., et al., 2020, *Nature Astronomy*, 4, 951
 Gillon M., et al., 2012, *A&A*, 542, A4
 Gordon I. E., Rothman L. S., Hargreaves R. J., et al., 2022, *J. Quant. Spectrosc. Radiat. Transfer*, 277, 107949
 Grant D., Lewis N. K., Wakeford H. R., Batalha N. E., et al., 2023, *ApJ*, 956, L32

- He M., 2013, *Electronic Structures and Optical Properties of Wollastonite*. Advanced Materials Research Vol. 815, Trans Tech Publications Ltd, doi:10.4028/www.scientific.net/AMR.815.183
- Hellier C., et al., 2011, *A&A*, 535, L7
- Helling C., Woitke P., 2006, *A&A*, 455, 325
- Helling C., et al., 2008a, *Mon. Not. R. Astron. Soc.*, 391, 1854
- Helling C., Woitke P., Thi W. F., 2008b, *A&A*, 485, 547
- Helling C., Kawashima Y., Graham V., Samra D., Chubb K. L., Min M., Waters L. B. F. M., Parmentier V., 2020, *A&A*, 641, A178
- Helling C., et al., 2021, *A&A*, 649, A44
- Helling C., et al., 2023, *A&A*, 671, A122
- Heng K., Demory B.-O., 2013, *ApJ*, 777, 100
- Heng K., Morris B. M., Kitzmann D., 2021, *Nature Astronomy*, 5, 1001
- Henning T., Begemann B., Mutschke H., Dorschner J., 1995, *Astron. Astrophys. Suppl. Ser.*, 112, 143
- Howarth I. D., 2011, *Mon. Not. R. Astron. Soc.*, 418, 1165
- Hoyer S., et al., 2023, *A&A*, 675, A81
- Jacobs B., et al., 2023, *ApJ Letters*, 956, L43
- Jäger C., Dorschner J., Mutschke H., Posch T., Henning T., 2003, *A&A*, 408, 193
- Kataria T., Showman A. P., Fortney J. J., Stevenson K. B., Line M. R., Kreidberg L., Bean J. L., Désert J.-M., 2015, *ApJ*, 801, 86
- Kopal Z., 1950, *Harvard College Observatory Circular*, 454, pp. 1-12, 454, 1
- Korth J., Parviainen H., 2024, *Universe*, 10
- Krenn A. F., et al., 2023, *A&A*, 672, A24
- Kurucz R., Bell B., 1995, *Kurucz atomic database*
- Lee E. K. H., Blecic J., Helling C., 2018, *A&A*, 614, A126
- Lee E. K. H., Parmentier V., Hammond M., Grimm S. L., Kitzmann D., Tan X., Tsai S.-M., Pierrehumbert R. T., 2021, *Mon. Not. R. Astron. Soc.*, 506, 2695
- Li L., et al., 2018, *Nature Communications*, 9, 3709
- Li G., Gordon I. E., Rothman L. S., Tan Y., Hu S.-M., Kassi S., Campargue A., Medvedev E. S., 2015, *Astrophys. J. Suppl.*, 216, 15
- Line M. R., Knutson H., Wolf A. S., Yung Y. L., 2014, *ApJ*, 783, 70
- Line M. R., et al., 2016, *AJ*, 152, 203
- Lodge M. G., Wakeford H. R., Leinhardt Z. M., 2023, *Mon. Not. R. Astron. Soc.*, 527, 11113
- Ma S., Ito Y., Al-Refaie A. F., Changeat Q., Edwards B., Tinetti G., 2023, *AJ*, 957, 104
- Madhusudhan N., Seager S., 2009, *ApJ*, 707, 24
- Mai C., Line M. R., 2019, *ApJ*, 883, 144
- McKemmish L. K., Yurchenko S. N., Tennyson J., 2016, *Mon. Not. R. Astron. Soc.*, 463, 771
- McKemmish L. K., Masseron T., Hoeijmakers H. J., Pérez-Mesa V., Grimm S. L., Yurchenko S. N., Tennyson J., 2019, *Mon. Not. R. Astron. Soc.*, 488, 2836
- Min M., Waters L. B. F. M., de Koter A., Hovenier J. W., Keller L. P., Markwick-Kemper F., 2007, *A&A*, 462, 667
- Min M., Ormel C. W., Chubb K., Helling C., Kawashima Y., 2020, doi:10.1051/0004-6361/201937377, 642, A28
- Mishchenko M. I., Dlugach J. M., Liu L., 2016, *J. Quant. Spectrosc. Radiat. Transfer*, 178, 284
- Mukherjee S., Batalha N. E., Marley M. S., 2021, *ApJ*, 910, 158
- Ohno K., Okuzumi S., Tazaki R., 2020, *ApJ*, 891, 131
- Pagano I., et al., 2023, *Constraining the reflective properties of WASP-178b using Cheops photometry (arXiv:2309.09037)*
- Palik E. D., 2012, *Handbook of Optical Constants of Solids: Vol 2*. Academic Press
- Palmer C., 2019, *Delft University of Technology Master Thesis*
- Parmentier V., Showman A. P., Lian Y., 2013, *A&A*, 558, A91
- Pinhas A., Madhusudhan N., 2017, *Mon. Not. R. Astron. Soc.*, 471, 4355
- Pollack J. B., Hollenbach D., Beckwith S., Simonelli D. P., Roush T., Fong W., 1994, *ApJ*, 421, 615
- Polyansky O. L., Kyuberis A. A., Zobov N. F., Tennyson J., Yurchenko S. N., Lodi L., 2018, *Mon. Not. R. Astron. Soc.*, 480, 2597
- Posch T., Kerschbaum F., Fabian D., Mutschke H., Dorschner J., Tamanai A., Henning T., 2003, *ApJSS*, 149, 437
- Robbins-Blanch N., Kataria T., Batalha N. E., Adams D. J., 2022, *ApJ*, 930, 93
- Roman M., Rauscher E., 2019, *ApJ*, 872, 1
- Rooney C. M., Batalha N. E., Gao P., Marley M. S., 2022, *ApJ*, 925, 33
- Samra D., Helling C., Min M., 2020, *A&A*, 639, A107
- Samra D., Helling C., Chubb K. L., Min M., Carone L., Schneider A. D., 2023, *A&A*, 669, A142
- Scandariato G., et al., 2022, *A&A*, 668, A17
- Schneider A. D., Carone L., Decin L., Jørgensen U. G., Mollière P., Baeyens R., Kiefer S., Helling C., 2022, *A&A*, 664, A56
- Stam D. M., 2008, *A&A*, 482, 989
- Stam D. M., Hovenier J. W., 2005, *A&A*, 444, 275
- Stam D. M., De Rooij W. A., Cornet G., Hovenier J. W., 2006, *A&A*, 452, 669
- Steinrueck M. E., Showman A. P., Lavvas P., Koskinen T., Tan X., Zhang X., 2021, *Mon. Not. R. Astron. Soc.*, 504, 2783
- Taylor J., Parmentier V., 2023, *Mon. Not. R. Astron. Soc.*, 526, 2133
- Torres G., Winn J. N., Holman M. J., 2008, *ApJ*, 677, 1324
- Triaud A., 2005, *Private Communication*
- Upadhyay A., Conway E. K., Tennyson J., Yurchenko S. N., 2018, *Mon. Not. R. Astron. Soc.*, 477, 1520
- Wakeford H. R., Sing D. K., 2015, *A&A*, 573, A122
- Woitke P., Helling C., 2003, *A&A*, 399, 297
- Woitke P., Helling C., 2004, *A&A*, 414, 335
- Woitke P., Helling C., Hunter G. H., Millard J. D., Turner G. E., Worters M., Blecic J., Stock J. W., 2018, *A&A*, 614, A1
- Yurchenko S. N., Amundsen D. S., Tennyson J., Waldmann I. P., 2017, *A&A*, 605, A95
- Yurchenko S. N., Bond W., Gorman M. N., Lodi L., McKemmish L. K., Nunn W., Shah R., Tennyson J., 2018, *Mon. Not. R. Astron. Soc.*, 478, 270
- Yurchenko S. N., Mellor T. M., Freedman R. S., Tennyson J., 2020, *Mon. Not. R. Astron. Soc.*, 496, 5282
- Yurchenko S. N., et al., 2021, *Mon. Not. R. Astron. Soc.*, 510, 903
- Zeidler S., Posch T., Mutschke H., Richter H., Wehrhan O., 2011, *A&A*, 526, A68
- Zellem R. T., et al., 2014, *ApJ*, 790, 53
- de Haan J. F., Bosma P., Hovenier J., 1987, *A&A*, 183, 371

APPENDIX A: LOG-NORMAL DERIVATION

We are going to consider the log-normal distribution written as a function of the particle radius a , the mean of the logarithm of particle size μ , the standard deviation of the logarithm of particle size σ , and particle number density n_d :

$$f(a; \mu, \sigma, n_d) = \frac{n_d}{a\sigma\sqrt{2\pi}} \exp\left(-\frac{(\ln(a) - \mu)^2}{2\sigma^2}\right). \quad (\text{A1})$$

Now we need to compute the moments of the distribution in radius-space of the cloud particles:

$$K_j = \int_{a_1}^{\infty} a^j f(a) da \quad (\text{A2})$$

where $f(a)$ is the distribution function of the cloud particles in radius a . We note that the units of this are $[\text{cm}^{-4}]$, where $[\text{cm}^{-1}]$ is from the distribution in radius-space, and $[\text{cm}^{-3}]$ is the number density of cloud particles (n_d) in the atmosphere. In other words, the integral of the distribution function is not normalised to 1. Hence, the moments in radius space have units of cm^j . For the log-normal distribution this is therefore:

$$K_j = \int_{a_1}^{\infty} a^j \frac{n_d}{a\sigma\sqrt{2\pi}} \exp\left(-\frac{(\ln(a) - \mu)^2}{2\sigma^2}\right) da. \quad (\text{A3})$$

To do this, we let $x = \ln(a)$, we also make the assumption $a_1 \rightarrow 0$. We note this is different from the assumption made in [Helling et al. \(2008b\)](#) for the Gaussian of $a_1 \rightarrow -\infty$, however the extension of the integral domain does not introduce a large error as, for both distributions, the function rapidly diminishes in these regions. Thus now with our change of units to x , we have limits of $\pm\infty$ and the integral becomes

$$K_j = \int_{-\infty}^{\infty} \frac{n_d}{\sigma\sqrt{2\pi}} \exp\left(jx - \frac{(x-\mu)^2}{2\sigma^2}\right) dx. \quad (\text{A4})$$

Next we focus on re-arranging the exponent in Eq. A4:

$$jx - \frac{(x-\mu)^2}{2\sigma^2} = \frac{1}{2\sigma^2} (2\sigma^2 jx - x^2 + 2x\mu - \mu^2). \quad (\text{A5})$$

First, we do the clever trick of introducing $(\mu + j\sigma^2)^2 - (\mu + j\sigma^2)^2$ inside the brackets. Then expanding the second part of this term, grouping like-terms of x , and cleaning up, we arrive at:

$$jx - \frac{(x-\mu)^2}{2\sigma^2} = \frac{1}{2\sigma^2} \left(-x^2 + 2(\mu + j\sigma^2)x - (\mu + j\sigma^2)^2 + j\sigma^2(2\mu + j\sigma^2) \right). \quad (\text{A6})$$

We recognise that by defining $\mu' = \mu + j\sigma^2$, the first three terms of the bracket reduce to simply $-(x^2 - \mu')^2$. Thus now substituting back into Eq. A4, we arrive at:

$$K_j = \exp\left(\frac{j(2\mu + j\sigma^2)}{2}\right) \int_{-\infty}^{\infty} \frac{n_d}{\sigma\sqrt{2\pi}} \exp\left(-\frac{(x-\mu')^2}{2\sigma^2}\right) dx, \quad (\text{A7})$$

where the integral is now just the integral over a Gaussian distribution (with the addition of the normalisation factor of n_d). Using the standard result:

$$\int_{-\infty}^{\infty} \exp(-c(x+b)^2) dx = \sqrt{\frac{\pi}{c}}, \quad (\text{A8})$$

where we let:

$$c = \frac{1}{2\sigma^2} \quad (\text{A9})$$

$$b = -\mu' \quad (\text{A10})$$

thus just the integral simplifies to:

$$\frac{n_d}{\sigma\sqrt{2\pi}} \int_{-\infty}^{\infty} \exp\left(-\frac{(x-\mu')^2}{2\sigma^2}\right) dx = \frac{n_d}{\sigma\sqrt{2\pi}} \sqrt{2\pi}\sigma = n_d. \quad (\text{A11})$$

This is a standard and expected result, given the normalisation of the moments K_j as discussed before. We therefore arrive (after far too much detail) at the expression for the K_j moment for a log-normal distribution:

$$K_j = n_d \exp\left(\frac{j(2\mu + j\sigma^2)}{2}\right). \quad (\text{A12})$$

Finally we derive a set of equations for the parameters n_d, μ, σ^2 , using the moments K_1, K_2, K_3 . We avoid the zeroth moment, K_0 , as it is used in the closure conditions of the moment equations, and therefore actually assumes a different form of the size distribution ([Helling et al. 2008b](#)). Taking the logarithm of Eq. A12:

$$\ln(K_j) = \ln(n_d) + \frac{j}{2}(2\mu + j\sigma^2), \quad (\text{A13})$$

and taking the difference of the logarithm of adjacent moments,

K_2, K_3 :

$$\begin{aligned} \ln(K_2) - \ln(K_1) &= (2\mu + 2\sigma^2) - \frac{1}{2}(2\mu + \sigma^2) \\ &= \mu + \frac{3}{2}\sigma^2 \end{aligned} \quad (\text{A14})$$

and

$$\begin{aligned} \ln(K_3) - \ln(K_2) &= \frac{3}{2}(2\mu + 3\sigma^2) - (2\mu + 2\sigma^2) \\ &= \mu + \frac{5}{2}\sigma^2. \end{aligned} \quad (\text{A15})$$

Then subtracting Eq. A14 from Eq. A15, we arrive at:

$$\sigma^2 = \ln(K_3) - 2\ln(K_2) + \ln(K_1). \quad (\text{A16})$$

Substituting this result back into Eq. A14 we get:

$$\ln(K_2) - \ln(K_1) = \mu + \frac{3}{2}(\ln(K_3) - 2\ln(K_2) + \ln(K_1)) \quad (\text{A17})$$

therefore

$$\mu = -\frac{3}{2}\ln(K_3) + 4\ln(K_2) - \frac{5}{2}\ln(K_1). \quad (\text{A18})$$

Finally, for n_d we take Eq. A16 and Eq. A18 for μ and σ^2 respectively, and substitute them into the formula for $\ln(K_2)$:

$$\begin{aligned} \ln(K_2) &= \ln(n_d) + 2\mu + 2\sigma^2 \\ &= \ln(n_d) \\ &\quad - 3\ln(K_3) + 8\ln(K_2) - 5\ln(K_1) \\ &\quad + 2\ln(K_3) - 4\ln(K_2) + 2\ln(K_1), \end{aligned} \quad (\text{A19})$$

simplifying, therefore:

$$\ln(n_d) = \ln(K_3) - 3\ln(K_2) + 3\ln(K_1). \quad (\text{A20})$$

Exponentiating this gives:

$$n_d = \frac{K_3 K_1^3}{K_2^3}. \quad (\text{A21})$$

So the final solution for the parameters for the log-normal distribution, in terms of radius-space moments K_1, K_2, K_3 are:

$$n_d = \frac{K_3 K_1^3}{K_2^3} \quad (\text{A22})$$

$$\mu = \ln\left(\frac{K_2^4}{\sqrt{K_3^3 K_1^5}}\right) \quad (\text{A23})$$

$$\sigma^2 = \ln\left(\frac{K_3 K_1}{K_2^2}\right). \quad (\text{A24})$$

APPENDIX B: ADDITIONAL FIGURES

This paper has been typeset from a $\text{\TeX}/\text{\LaTeX}$ file prepared by the author.

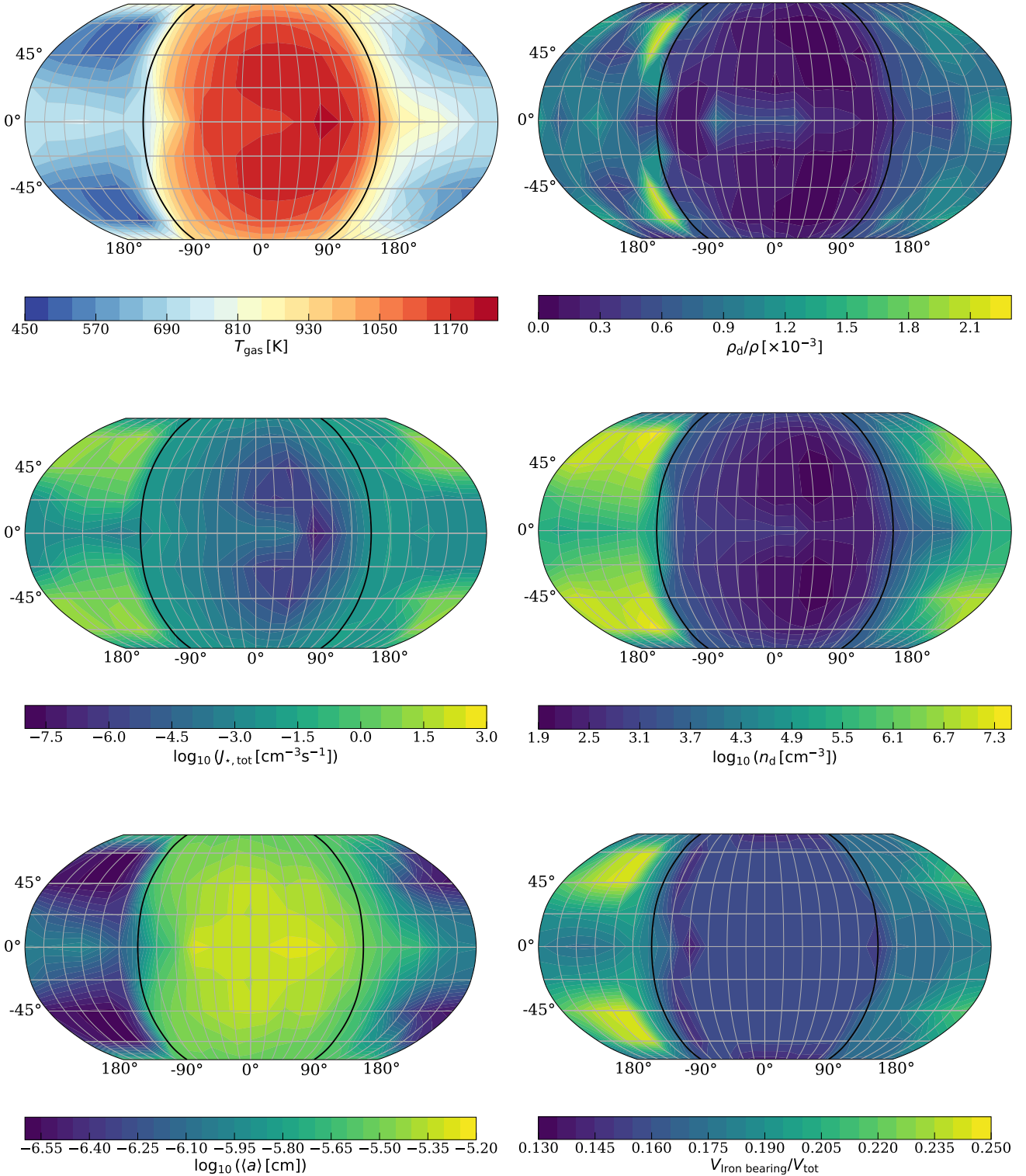


Figure B1. GCM and cloud formation results for WASP-43 b at $p_{\text{gas}} = 0.1$ mbar. The maps are centred on the substellar point ($\phi_{\text{long}} = 0^\circ$, $\lambda_{\text{lat}} = 0^\circ$), with the terminator limbs ($\phi_{\text{long}} = \pm 90^\circ$) shown in bold black lines. **Top Left:** The local gas temperature from the GCM solution. **Top Right:** Cloud particle mass load in the atmosphere as the ratio of the density of cloud particle mass to the gas density. **Middle Left:** Total nucleation rate. **Middle Right:** Cloud particle number density. **Bottom Left:** Average cloud particle size. **Bottom Right:** Volume fraction of the cloud particles composed of iron-bearing condensate species.

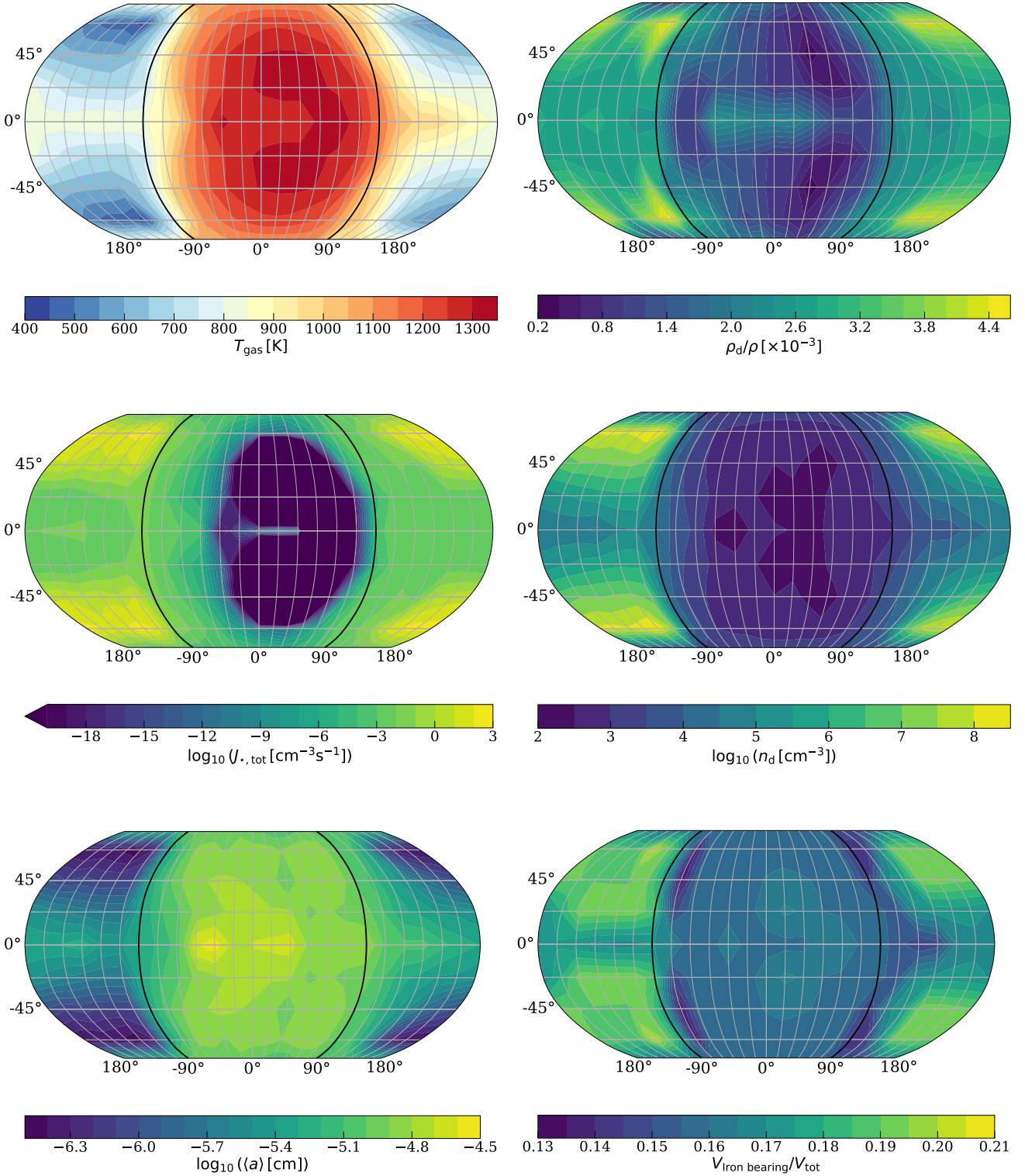


Figure B2. GCM and cloud formation results for WASP-43 b at $p_{\text{gas}} = 1$ mbar. The maps are centred on the substellar point ($\phi_{\text{long}} = 0^\circ$, $\lambda_{\text{lat}} = 0^\circ$), with the terminator limbs ($\phi_{\text{long}} = \pm 90^\circ$) shown in bold black lines. **Top Left:** The local gas temperature from the GCM solution. **Top Right:** Cloud particle mass load in the atmosphere as the ratio of the density of cloud particle mass to the gas density. **Middle Left:** Total nucleation rate. **Middle Right:** Cloud particle number density. **Bottom Left:** Average cloud particle size. **Bottom Right:** Volume fraction of the cloud particles composed of iron-bearing condensate species.

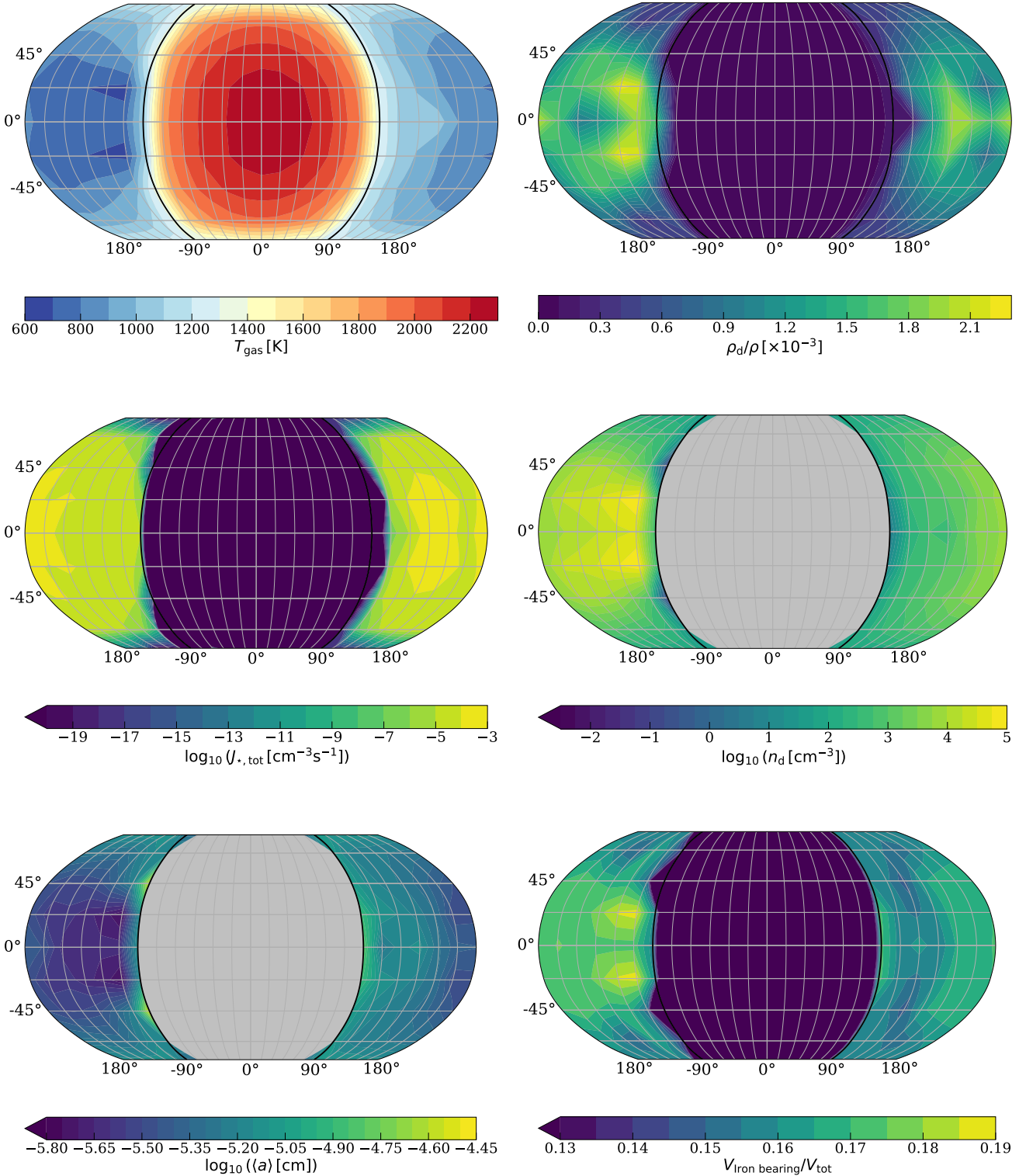


Figure B3. GCM and cloud formation results for HD 209458 b at $p_{\text{gas}} = 0.1$ mbar. The maps are centred on the substellar point ($\phi_{\text{long}} = 0^\circ$, $\lambda_{\text{lat}} = 0^\circ$), with the terminator limbs ($\phi_{\text{long}} = \pm 90^\circ$) shown in bold black lines. **Top Left:** The local gas temperature from the GCM solution. **Top Right:** Cloud particle mass load in the atmosphere as the ratio of the density of cloud particle mass to the gas density. **Middle Left:** Total nucleation rate. **Middle Right:** Cloud particle number density. **Bottom Left:** Average cloud particle size. **Bottom Right:** Volume fraction of the cloud particles composed of iron-bearing condensate species.

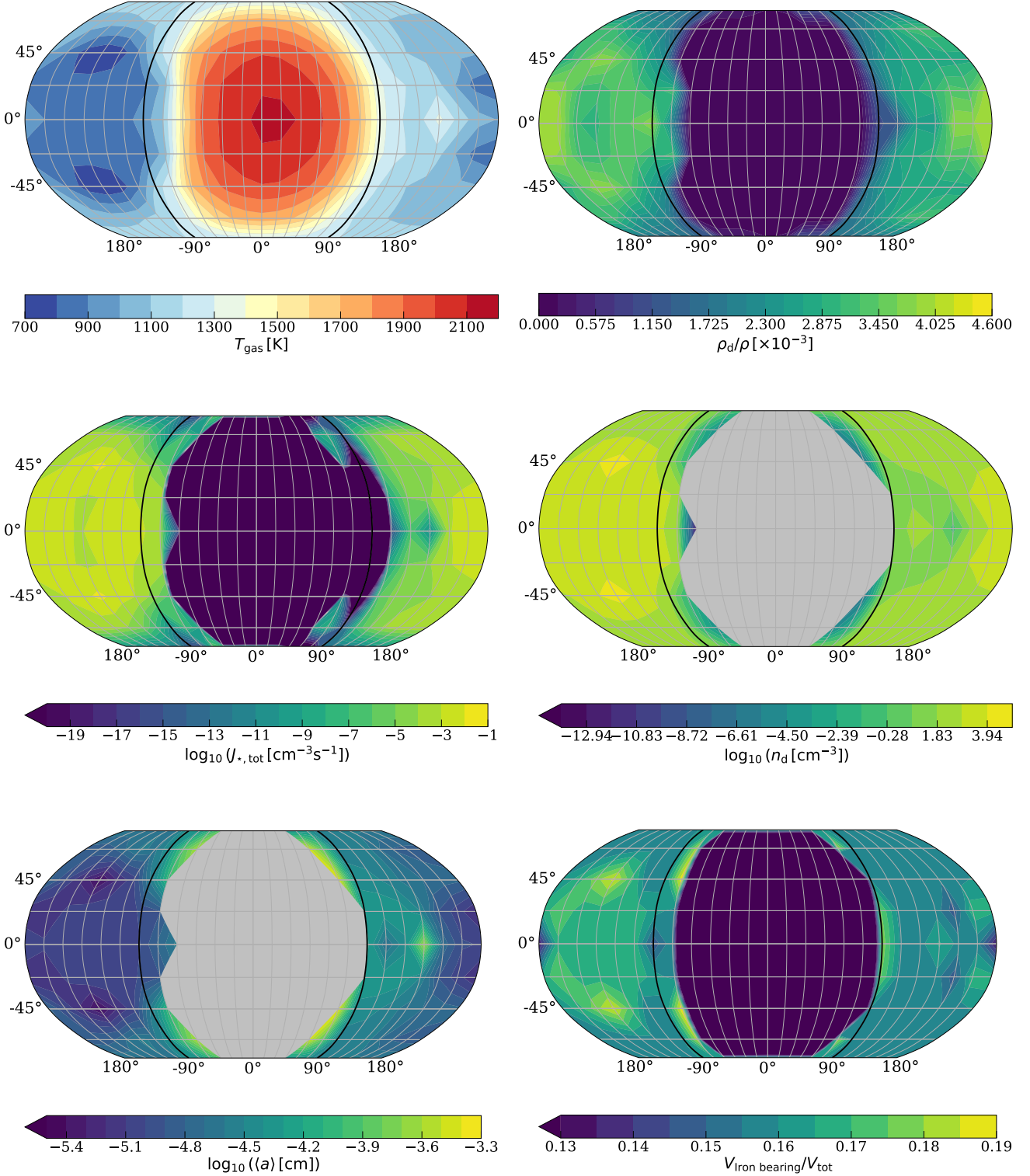


Figure B4. GCM and cloud formation results for HD 209458 b at $p_{\text{gas}} = 1$ mbar. The maps are centred on the substellar point ($\phi_{\text{long}} = 0^\circ$, $\lambda_{\text{lat}} = 0^\circ$), with the terminator limbs ($\phi_{\text{long}} = \pm 90^\circ$) shown in bold black lines. **Top Left:** The local gas temperature from the GCM solution. **Top Right:** Cloud particle mass load in the atmosphere as the ratio of the density of cloud particle mass to the gas density. **Middle Left:** Total nucleation rate. **Middle Right:** Cloud particle number density. **Bottom Left:** Average cloud particle size. **Bottom Right:** Volume fraction of the cloud particles composed of iron-bearing condensate species.

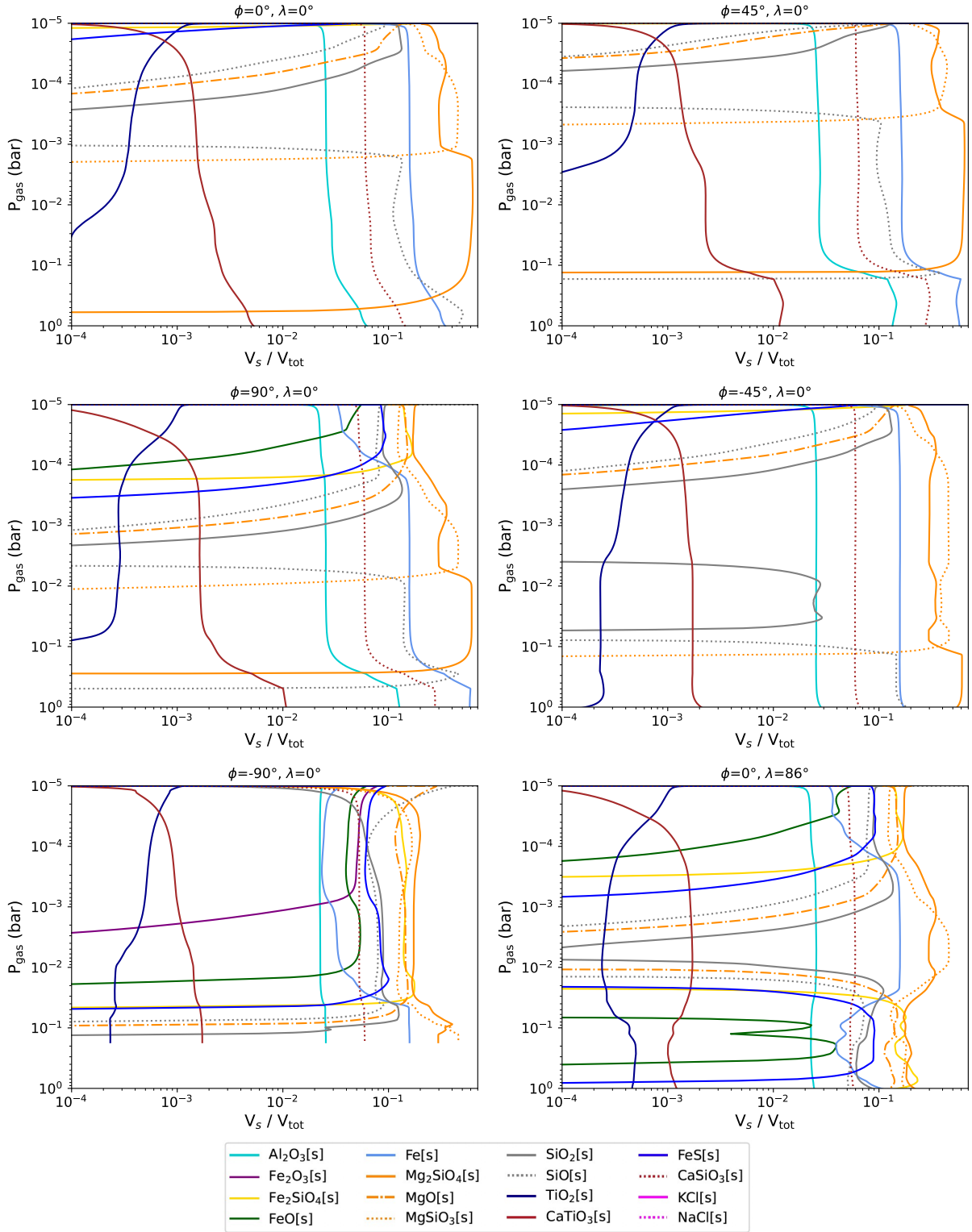


Figure B5. Material volume fractions V_s / V_{tot} of the different materials forming the mixed-material cloud particles for WASP-43 b at the longitude, latitude specified in each panel.

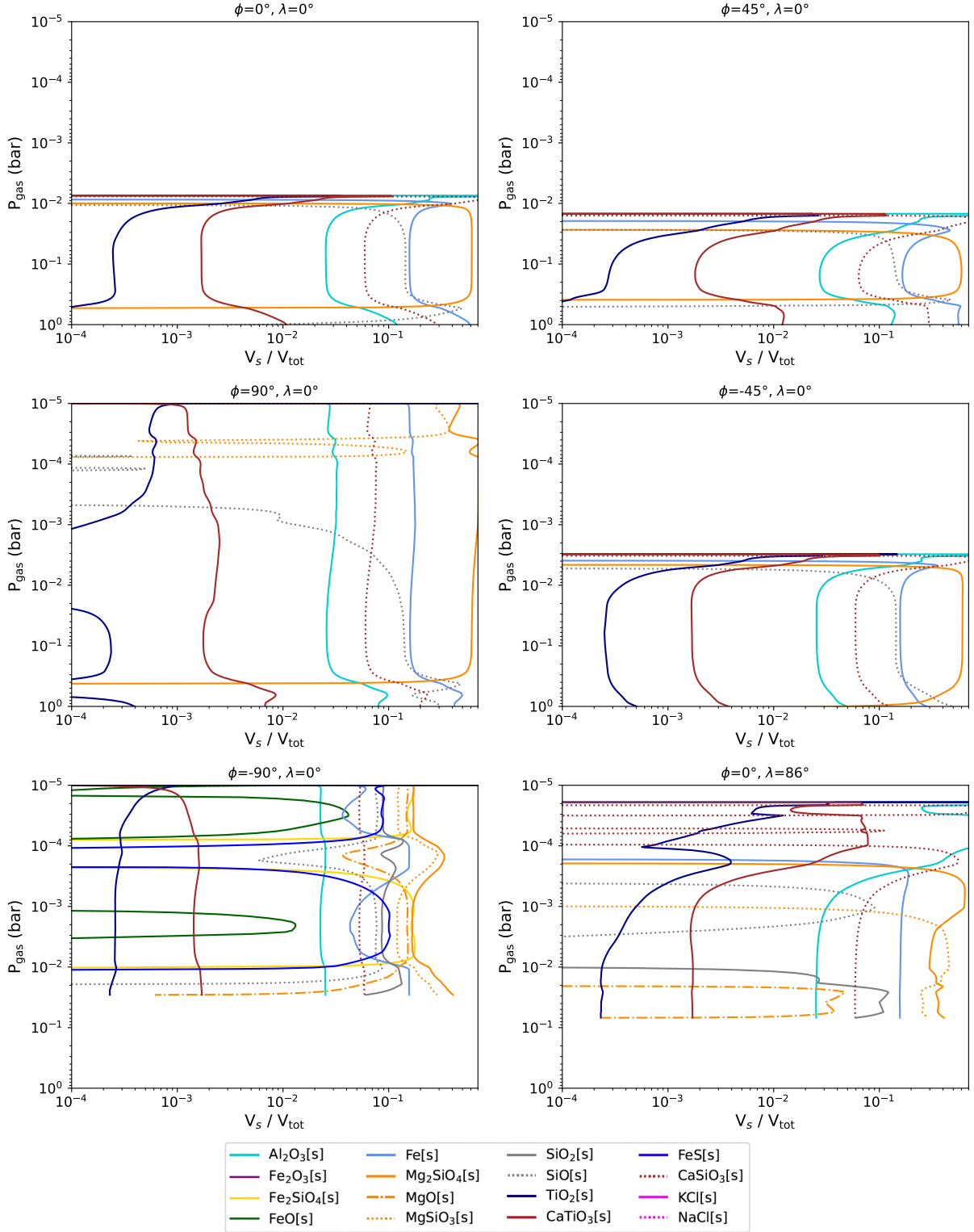


Figure B6. Material volume fractions V_s / V_{tot} of the different materials forming the mixed-material cloud particles for HD 209458 b at the longitude, latitude specified in each panel.

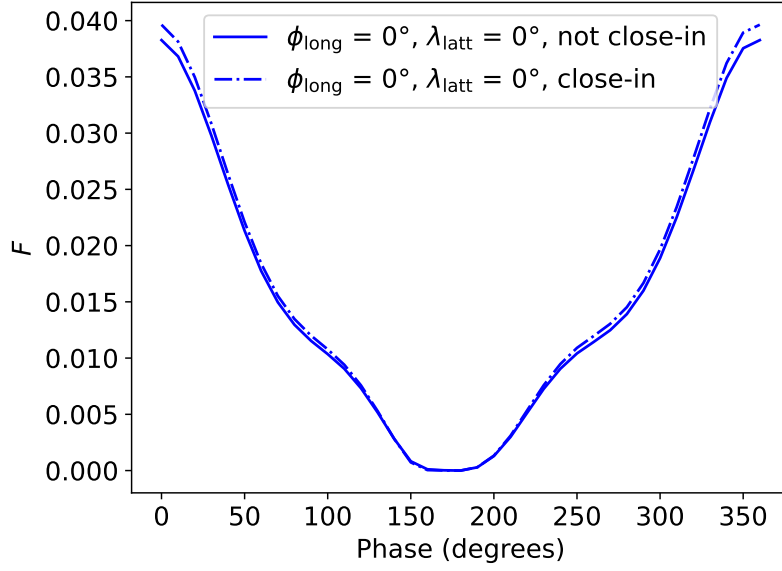


Figure B7. A comparison of before the amendments for close-in exoplanets were made (solid line) to after (dash-dotted line) for a horizontally homogeneous atmosphere of WASP-43 b modelled using the atmosphere at the sub-solar point.

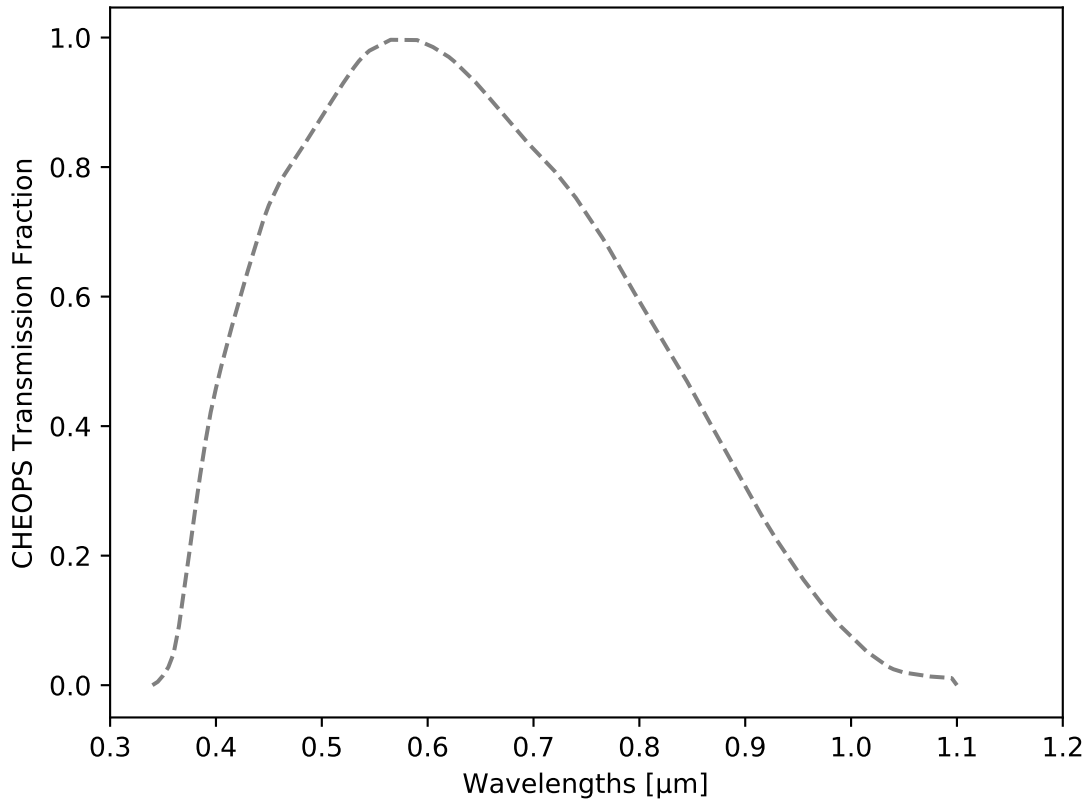


Figure B8. Transmission fraction for the CHEOPS bandpass taken from <http://svo2.cab.inta-csic.es/theory/fps/>, taking into account both filter throughput and CCD sensitivity.

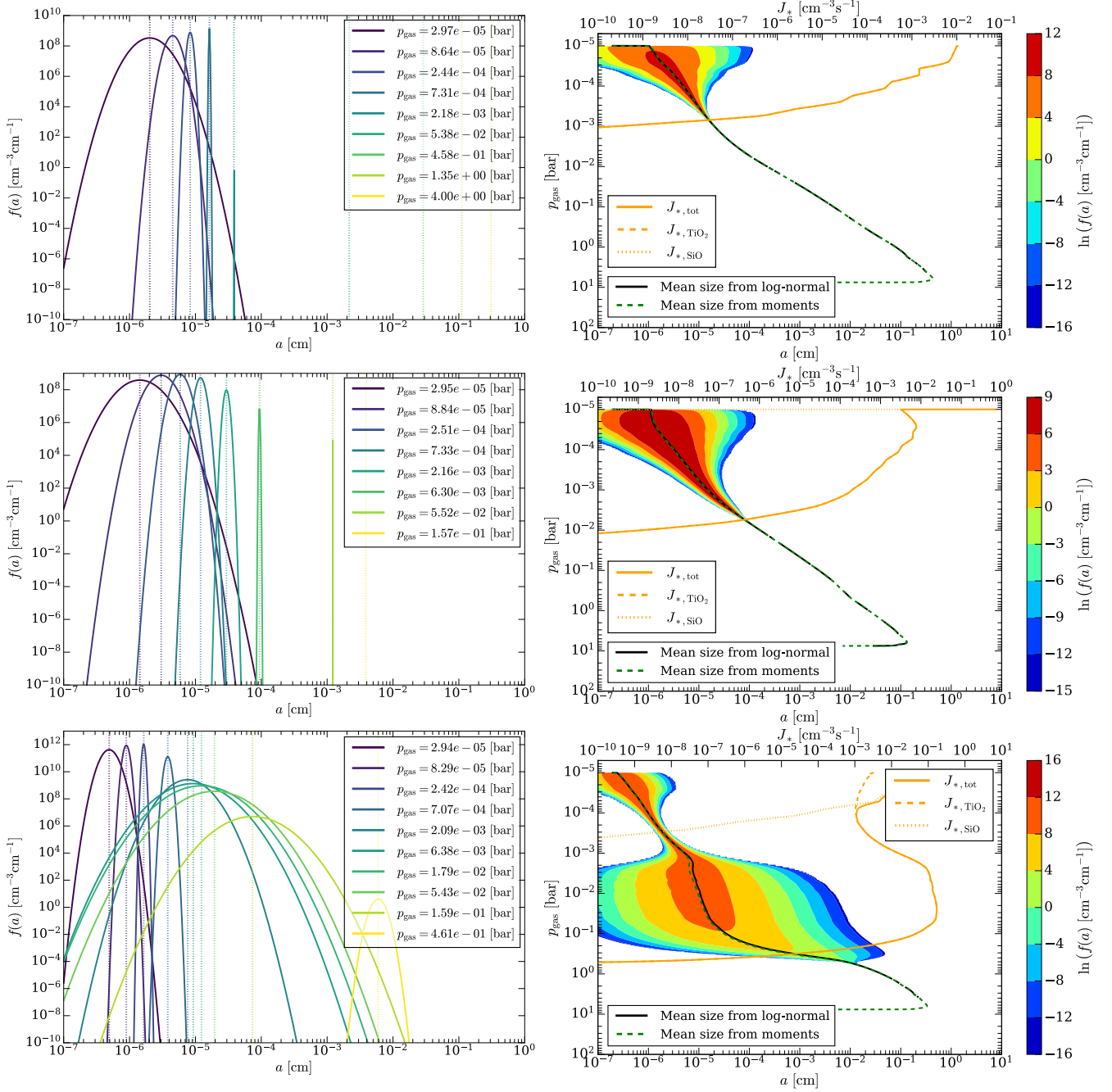


Figure B9. Log-normal distribution for WASP 43b for points at the equator ($\lambda = 0^\circ$) from top to bottom these show the substellar point, evening terminator, and the morning terminator. **Left:** The derived log-normal size distribution function for individual pressure levels through the atmosphere, dotted lines indicate the average particle size, in the case that the distribution becomes monodisperse (i.e. that no valid solution for the log-normal parameters exists), only the average particle size is shown. **Right:** Cloud Particle size distribution as contours against pressure. The average particle size from the log-normal is shown as a black line. The average particle size derived from the moments ($\langle a \rangle = (3/4\pi)^{1/3} L_1/L_0$) is shown in dashed green, showing good agreement at all pressures. Also over-plotted in orange are the nucleation rates, indicating that the log-normal size distribution broadens in regions with efficient nucleation, in order to capture the presence of the population of small cloud particles resulting ‘recently nucleated’ particles that have not yet undergone substantial particle growth.

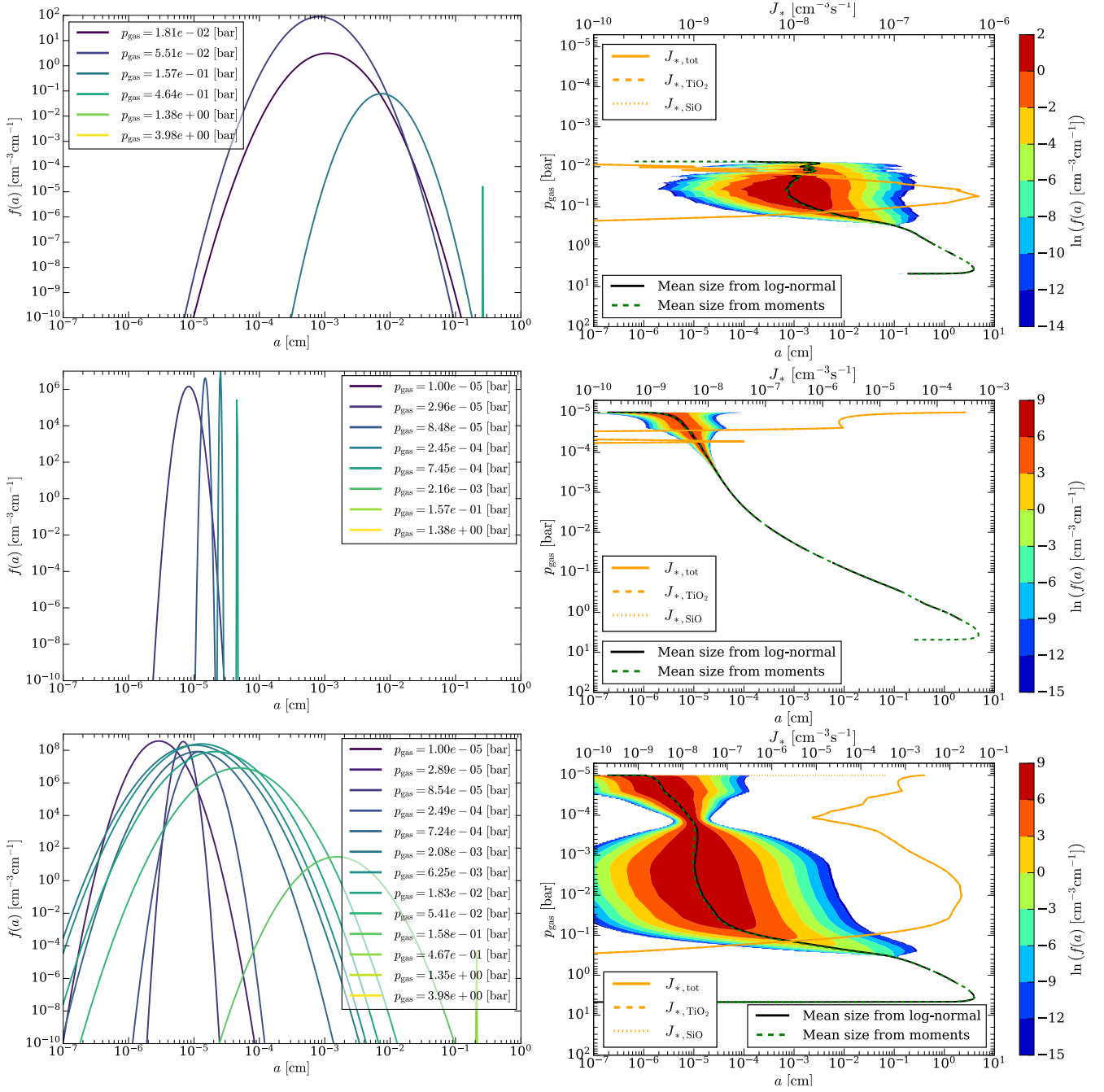


Figure B10. Log-normal distribution for HD209458 b for points at the equator ($\lambda = 0^\circ$) from top to bottom these show the substellar point, evening terminator, and the morning terminator. **Left:** The derived log-normal size distribution function for individual pressure levels through the atmosphere, dotted lines indicate the average particle size. **Right:** Cloud Particle size distribution as contours against pressure. The average particle size from the log-normal is shown as a black line. The average particle size derived from the moments is shown in dashed green. Also over-plotted in orange are the nucleation rates.